An International Journal of Optimization and Control: Theories & Applications
ISSN: 2146-0957 eISSN: 2146-5703
Vol.16, No.6, pp.2194-2217 (2026)
https://doi.org/10.36922/IJOCTA026250123

RESEARCH ARTICLE

A kernel-adaptive Mittag-Leffler polynomial framework for ψ-Caputo fractional optimal control of robotic systems

Amin Jajarmi[1,2*] and Dumitru Baleanu[3,4]

[1]Department of Electrical Engineering, University of Bojnord, Bojnord, Iran
[2]Department of Mathematics, Saveetha School of Engineering, Saveetha Institute of Medical and Technical Sciences, Saveetha University, Chennai, Tamil Nadu, India
[3]Department of Computer Science and Mathematics, Lebanese American University, Beirut, Lebanon
[4]Institute of Space Sciences, Magurele, Bucharest, Romania
a.jajarmi@ub.ac.ir, dumitru.baleanu@lau.edu.lb

ARTICLE INFO

Article History:
Received: June 18, 2026
Revised: August 20, 2026
Accepted: August 25, 2026
Published Online: September 29, 2026

Keywords:
Operational-time transformation
Kernel sensitivity
Reduced-space optimization
Quadratic programming
Numerical conditioning

AMS Classification:
26A33; 49M25; 49N10

ABSTRACT

This paper develops a kernel-adaptive Mittag-Leffler polynomial framework for solving ψ-Caputo fractional optimal-control problems arising in robotic systems. In the proposed formulation, the function ψ is interpreted as a nonlinear operational clock that reshapes the memory structure of the fractional dynamics and influences the distribution of the control effort over physical time. A normalized operational-time transformation is introduced to convert the original ψ-Caputo system into an equivalent Caputo-type representation; at the same time, the physical-time performance index is preserved through the inverse-clock Jacobian. This formulation allows different kernel choices to be incorporated systematically without altering the underlying optimal control structure. For numerical implementation, QR-orthonormalized Mittag-Leffler polynomial bases are constructed to improve stability and conditioning. The fractional integral terms are evaluated analytically by expanding the basis functions in terms of monomials, yielding an efficient finite-dimensional approximation. For the linear planar robotic regulator, the state variables are analytically eliminated, yielding a symmetric positive-definite quadratic programming problem. For the nonlinear two-link manipulator, the same transformation and approximation strategy produce a nonlinear programming formulation. The method is first validated using a manufactured ψ-Caputo benchmark problem, confirming its accuracy and consistency. It is then applied to robotic control examples to examine the effects of kernel selection on terminal accuracy, control energy, physical-time cost, peak actuation, torque profiles, and numerical conditioning. The results demonstrate that the operational clock significantly influences both computational performance and control behavior.

CC BY

1. Introduction

Optimization-based control provides a common mathematical framework for trajectory planning, stabilization, control allocation, and constrained decision-making in robotic systems. Modern formulations generally combine a dynamic model, a performance index, boundary conditions, and state or input constraints to determine optimal state-control trajectories. This perspective has become particularly important for systems characterized by strong coupling, limited energy resources, and long-range temporal dependencies. Fractional calculus has therefore emerged as a fundamental tool for modeling such systems due to its ability to incorporate memory, hereditary effects, and nonlocal temporal behavior in dynamical processes. Fractional-order systems explicitly incorporate history-dependent dynamics, unlike

*Corresponding Author

classical integer-order models.[1] Such are are beneficial for robotics, viscoelastic materials, diffusion processes, and control systems.[2]

Fractional calculus has been widely used to model dynamical systems with memory effects; its mathematical foundations were laid in classical works such as Samko *et al.*[3] and Baleanu *et al.*,[4] which also discuss its physical interpretation through fractional differential equations. Fractional optimal-control problems (FOCPs) were systematically formulated in the optimal-control literature by Agrawal[5] and subsequently extended by Baleanu *et al.*[6] using variational and generalized dynamic frameworks. The numerical treatment of fractional-order systems has also been studied extensively,[7,8] especially by spectral and collocation methods (see, e.g.,[9,10]). Stable high-order iterative solvers for nonlinear equations have further been developed.[11] Moreover, stability analysis remains an important topic, with Mittag-Leffler stability playing a central role.[12] Later extensions considered fractional systems with delays.[13] Additionally, efficient numerical solutions of FOCPs have been considered in recent works.[14–17] Fractional-order systems have also been used to model memory-dependent phenomena in extensions of neural control systems[18] and robotics.[19–21] However, many existing approaches still depend on prescribed fractional kernels, which may not be appropriate for representing systems with adaptive time scaling and non-uniform memory structures. This limits the flexibility to model complex dynamical systems, especially robotics, where dynamic environments and sensitivity to control inputs require flexible temporal representations. This has motivated the introduction of generalized fractional operators, including exponential-extension-kernel derivatives[22] and operators with respect to another function ψ,[23] such as the ψ-Caputo derivative.[24] For a strictly increasing function ψ, the ψ-Caputo derivative replaces the classical time difference $t-s$ with the operational lag $\psi(t)-\psi(s)$, thereby defining differentiation with respect to the temporal scale generated by ψ. This construction includes the classical Caputo and Caputo-Hadamard operators as special cases and recovers inverse relations, integration-by-parts formulas, and various approximation tools,[24,25] while preserving several structural properties of fractional integrals under suitable conditions. Importantly, changing ψ is not a purely notational modification; it changes the operational clock on which memory is measured. After the inverse transformation $t=\chi(\theta)$, where θ denotes normalized operational time and χ is the corresponding inverse map, the same clock also enters the objective through a Jacobian density. Consequently, even endpoint-normalized clocks may yield different running-cost weights, optimal control-effort distributions, terminal accuracies, and total physical-time costs. Almeida's population model example already demonstrated that kernel choice can significantly affect model fidelity.[26] These observations also distinguish the present work from related lines of research. Conventional FOCP formulations generally optimize state-control trajectories after the fractional operator or memory kernel has been prescribed.[5,6] In particular, relative to existing ψ-Caputo FOCP formulations such as,[6] the mathematical distinction of the present framework does not lie in the introduction of the ψ-Caputo operator itself. Rather, it lies in the explicit normalized pullback $\theta=(\psi(t)-\psi(0))/\Delta_\psi$, which transforms the ψ-Caputo state dynamics into a standard Caputo form in operational time, with the factor Δ_ψ^α appearing on the right-hand side of the transformed state equation, while preserving the original physical-time objective through the inverse-clock Jacobian $\chi'(\theta)$. The resulting operational-time problem is then discretized using the reduced-space Mittag-Leffler formulation. Spectral, collocation, Galerkin, Chebyshev, Legendre, and Mittag-Leffler polynomial methods primarily define approximation spaces or discretization rules for fractional equations and FOCPs.[9,10,15,16,21] Fractional linear-quadratic control methods exploit linear dynamics and quadratic costs for a prescribed fractional model or fixed-kernel representation.[27–29] By contrast, the present work treats ψ as a model-level operational clock: it changes the memory geometry through $\psi(t)-\psi(s)$ and $\psi'(t)$, and it modifies the physical-time objective through the inverse-clock Jacobian $\chi'(\theta)$. Thus, the issue addressed here is not simply how to discretize an FOCP, but how to formulate and solve a kernel-adaptive robotic FOCP in which the kernel influences memory distribution, cost density, actuation allocation, terminal accuracy, and numerical conditioning. **Table 1** summarizes the main distinctions between the proposed framework and the related classes of methods discussed above. To the best of the authors' knowledge, a unified framework combining (i) the operational-time transformation of the ψ-Caputo dynamics, (ii) Jacobian-consistent preservation of the original physical-time performance index, (iii) QR-stabilized Mittag-Leffler polynomial approximation with analytical fractional-integral evaluation, and (iv) robotic sensitivity analysis with respect to kernel choice has not been systematically developed.

Motivated by these gaps, the main contributions of this work are summarized as follows:

- A kernel-adaptive ψ-Caputo FOCP framework is developed in which ψ is treated as a model-level operational clock for robotic systems, rather than as a passive notation change or a fixed prescribed kernel.
- A normalized operational-time transformation is used to transform the ψ-Caputo dynamics while preserving the original physical-time performance index through the inverse-clock Jacobian $\chi'(\theta)$.
- The four distinct operational effects of ψ are separated explicitly: memory redistribution through $\psi(t) - \psi(s)$ and $\psi'(t)$, physical-time cost weighting through $\chi'(\theta)$, clock-dependent control-effort allocation, and clock-dependent terminal accuracy.
- A QR-orthonormalized Mittag-Leffler polynomial basis is embedded inside the transformed ψ-Caputo FOCP, so that the basis is used not only as a standalone spectral approximation but as part of a kernel-adaptive optimal-control discretization.
- An analytical monomial-based representation of fractional integrals is derived, enabling exact fractional-integral evaluation in the polynomial approximation space, up to floating-point arithmetic.
- For the linear planar regulator, the clock-dependent reduced algebraic structure is derived explicitly; after state elimination, the discretized linear-quadratic benchmark becomes a symmetric positive-definite quadratic program with Jacobian-weighted physical-time quadrature.
- The scope of the quadratic reduction is delimited by the nonlinear two-link manipulator validation case, where the same ψ-Caputo transformation and Mittag-Leffler approximation lead to a finite-dimensional NLP problem rather than a quadratic program.
- A kernel-selection discussion and a continuous ψ_ρ sensitivity sweep, where ρ denotes the clock-shape parameter, quantify how clock shape affects memory distribution, physical-time cost, terminal accuracy, control energy, peak actuation, and conditioning in the robotic examples considered.

Table 1. Comparison of the proposed framework with related methods

Related approach	Main distinction of the proposed framework
Fixed-kernel FOCPs	Many FOCP formulations optimize trajectories after the fractional operator or memory kernel has been prescribed. Here, ψ is treated as an operational clock that changes memory geometry, physical-time cost density, actuation allocation, and terminal accuracy.
ψ-Caputo FOCP formulations	The ψ-Caputo operator is already available for fractional optimal-control modeling.[6] Here, the normalized pullback converts the ψ-Caputo dynamics to a Caputo form in θ while the original physical-time objective is retained through $\chi'(\theta)$; the resulting problem is then discretized in operational time.
Spectral and polynomial methods	Spectral and polynomial methods typically provide approximation spaces or discretization rules. Here, the QR-stabilized Mittag-Leffler basis is embedded inside the ψ-Caputo operational-time reformulation with analytical fractional-integral evaluation.
Fractional LQ control	Fractional LQ methods typically analyze a prescribed fractional model with linear dynamics and quadratic cost. Here, the linear regulator exposes a clock-dependent reduced quadratic system with Jacobian-weighted physical-time quadrature induced by ψ.
Fractional robotic control	Many fractional robotic-control studies select a fractional order or kernel before simulation. Here, we compare admissible clocks to quantify their effects on cost, terminal error, control energy, peak actuation, torque profiles, and conditioning.

The remainder of this paper is organized as follows. Section 2 presents preliminaries on fractional calculus and Mittag-Leffler functions. Section 3 formulates the ψ-Caputo optimal control problem. Section 4 develops the numerical discretization and reduction methodology. Section 5 provides theoretical and computational analysis. Section 6

describes numerical experiments. Section 7 concludes the paper.

2. Mathematical preliminaries

2.1. ψ-fractional integral and derivative

Let $I = [0, T]$ be the physical-time interval, where $T > 0$ is the final time; let $0 < \alpha \leq 1$ be the fractional order; and assume that the operational-clock function $\psi \in C^1(I)$ is strictly increasing with $\psi'(t) > 0$ on I. For an integrable scalar or vector function f, the left fractional integral with respect to ψ is:[24,30]

$$(I_{0+}^{\alpha,\psi} f)(t) = \frac{1}{\Gamma(\alpha)} \int_0^t \psi'(s)\big(\psi(t) - \psi(s)\big)^{\alpha-1} f(s)\, ds. \tag{1}$$

Here, $\Gamma(\cdot)$ denotes the Gamma function. For $f \in C^1(I)$ and $0 < \alpha < 1$, the left ψ-Caputo derivative is:

$$({}^{C}D_{0+}^{\alpha,\psi} f)(t) = \frac{1}{\Gamma(1-\alpha)} \int_0^t \big(\psi(t) - \psi(s)\big)^{-\alpha} f'(s)\, ds. \tag{2}$$

For $\alpha = 1$, it is defined by:

$$({}^{C}D_{0+}^{1,\psi} f)(t) = \frac{1}{\psi'(t)} \frac{df}{dt}(t). \tag{3}$$

For vector-valued functions, these operators are understood componentwise. For $f \in C^1(I)$ and $0 < \alpha \leq 1$, the inverse identity needed below is:

$$\big(I_{0+}^{\alpha,\psi}[{}^{C}D_{0+}^{\alpha,\psi} f]\big)(t) = f(t) - f(0). \tag{4}$$

Moreover, for $\alpha, \beta > 0$, the corresponding fractional integrals satisfy the semigroup law:

$$I_{0+}^{\alpha,\psi}\big(I_{0+}^{\beta,\psi} f\big) = I_{0+}^{\alpha+\beta,\psi} f, \tag{5}$$

whenever the involved integrals exist. These relations are central because they permit state reconstruction from an approximation of the control or the fractional derivative.

Remark 1. *When $\psi(t) = t$, **Equations (1)–(2)** reduce to the standard Riemann-Liouville fractional integral and Caputo fractional derivative.[31] If the problem is instead posed on a positive interval $[a, T]$, with $a > 0$, and $\psi(t) = \log t$, then a Caputo-Hadamard type operator is obtained. Alternatively, on $[0, T]$, one may use a shifted logarithmic clock such as $\psi(t) = \log(t + a)$ with $a > 0$. Alternative fractional formulations used in recent nonlinear models include the M-fractional derivative,[32] the conformable fractional derivative,[33] and the beta fractional derivative;[34] these operators constitute distinct fractional-derivative definitions from the nonlocal ψ-Caputo derivative considered in the present work. Other admissible choices of ψ produce nonlinear operational clocks without changing the fractional order α.[24,35] Thus, α fixes the strength of the nonlocal power-law memory, whereas ψ fixes the clock on which that memory is measured. In particular, a large value of $\psi'(t)$ makes the operational clock advance rapidly over that part of the physical maneuver; a small value of $\psi'(t)$, on the other hand, makes the operational clock advance slowly. Therefore, ψ controls the temporal placement of memory effects independently of the fractional order.*

2.2. Normalized operational time

Define:

$$\Delta_\psi = \psi(T) - \psi(0), \qquad \theta = \Theta(t) = \frac{\psi(t) - \psi(0)}{\Delta_\psi}, \quad \theta \in [0, 1]. \tag{6}$$

The inverse map is denoted by $t = \chi(\theta) = \Theta^{-1}(\theta)$. For a physical-time function $f(t)$, define its pullback:

$$\widehat{f}(\theta) = f(\chi(\theta)). \tag{7}$$

Because Θ is strictly increasing:

$$\chi'(\theta) = \frac{\Delta_\psi}{\psi'(\chi(\theta))}, \quad \chi'(\theta) > 0. \tag{8}$$

Theorem 1 (Operational-time pullback)**.** *Let $0 < \alpha \leq 1$ and let $f \in C^1([0, T])$ such that all involved fractional integrals are well-defined. Then:*

$$({}^{C}D_{0+}^{\alpha,\psi} f)(t) = \Delta_\psi^{-\alpha}({}^{C}D_{0+}^{\alpha} \widehat{f})(\Theta(t)), \tag{9}$$

where ${}^{C}D_{0+}^{\alpha}$ is the standard Caputo derivative on $[0, 1]$. Moreover:

$$(I_{0+}^{\alpha,\psi} f)(t) = \Delta_\psi^{\alpha}(I_{0+}^{\alpha} \widehat{f})(\Theta(t)). \tag{10}$$

Proof. For the integral identity, set $\sigma = (\psi(s) - \psi(0))/\Delta_\psi$ in **Equation (1)**. Then, $d\sigma = \psi'(s)ds/\Delta_\psi$ and $\psi(t) - \psi(s) = \Delta_\psi(\Theta(t) - \sigma)$. Hence:

$$\begin{aligned}(I_{0+}^{\alpha,\psi} f)(t) &= \frac{\Delta_\psi^{\alpha}}{\Gamma(\alpha)} \int_0^{\Theta(t)} (\Theta(t) - \sigma)^{\alpha-1} \widehat{f}(\sigma)\, d\sigma \\ &= \Delta_\psi^{\alpha}(I_{0+}^{\alpha} \widehat{f})(\Theta(t)).\end{aligned} \tag{11}$$

For the derivative identity, the same substitution gives:

$$\begin{aligned}&({}^{C}D_{0+}^{\alpha,\psi} f)(t) \\ &= \frac{1}{\Gamma(1-\alpha)} \int_0^t (\psi(t) - \psi(s))^{-\alpha} f'(s)\, ds \\ &= \Delta_\psi^{-\alpha} \frac{1}{\Gamma(1-\alpha)} \int_0^{\Theta(t)} (\Theta(t) - \sigma)^{-\alpha} \widehat{f}'(\sigma)\, d\sigma \\ &= \Delta_\psi^{-\alpha}({}^{C}D_{0+}^{\alpha} \widehat{f})(\Theta(t)).\end{aligned} \tag{12}$$

This proves **Equations (9)** and **(10)**. □

Theorem 1 makes the role of ψ explicit. The variable θ is the normalized operational time generated by the clock ψ, not merely an auxiliary

numerical coordinate. In the memory kernel, the physical-time lag is replaced by the operational lag:

$$\psi(t) - \psi(s) = \Delta_\psi\big(\Theta(t) - \Theta(s)\big). \tag{13}$$

Thus, the clock rate:

$$\frac{d\theta}{dt} = \frac{\psi'(t)}{\Delta_\psi}, \tag{14}$$

determines how each physical-time interval is represented in operational memory. If $\Delta_\psi = 1$, the multiplicative scaling in **Equation (9)** disappears and the fractional derivative takes the standard Caputo form in θ. However, this normalization does not remove the effect of the clock. Physical-time coefficients, states, and controls must still be pulled back through $t = \chi(\theta)$, and every physical-time integral transforms according to the following:

$$\begin{aligned} \int_0^T g(t)\,dt &= \int_0^1 g(\chi(\theta))\chi'(\theta)\,d\theta, \\ \chi'(\theta) &= \frac{\Delta_\psi}{\psi'(\chi(\theta))}. \end{aligned} \tag{15}$$

Consequently, normalized clocks with identical endpoint values may still yield different memory distributions, running-cost weights, optimal control-effort distributions, terminal accuracies, and physical-time costs.

2.3. Mittag-Leffler polynomials

The exponential generating function defines the normalized Mittag-Leffler polynomials used in this work:

$$\sum_{m=0}^{\infty} M_m(\theta)\frac{\zeta^m}{m!} = \left(\frac{1+\zeta}{1-\zeta}\right)^\theta, \quad |\zeta| < 1, \tag{16}$$

where ζ is an auxiliary generating variable. Under this normalization, they form an associated Sheffer sequence.[21,36] Differentiating **Equation (16)** with respect to ζ gives:

$$(1-\zeta^2)\frac{\partial}{\partial\zeta}\left(\frac{1+\zeta}{1-\zeta}\right)^\theta = 2\theta\left(\frac{1+\zeta}{1-\zeta}\right)^\theta. \tag{17}$$

This follows from direct differentiation of **Equation (16)** and algebraic simplification. Comparison of coefficients yields recurrence relations:

$$M_0(\theta) = 1, \quad M_1(\theta) = 2\theta, \tag{18}$$

and for $m \geq 1$:

$$M_{m+1}(\theta) = 2\theta M_m(\theta) + m(m-1)M_{m-1}(\theta). \tag{19}$$

The first members are:

$$M_0(\theta) = 1, \quad M_1(\theta) = 2\theta, \quad M_2(\theta) = 4\theta^2, \tag{20}$$

$$M_3(\theta) = 8\theta^3 + 4\theta, \quad M_4(\theta) = 16\theta^4 + 32\theta^2. \tag{21}$$

Since $\deg M_m = m$ and, from the recurrence relation, the leading coefficient satisfies $\gamma_{m+1} = 2\gamma_m$ with $\gamma_0 = 1$, it follows that $\gamma_m = 2^m$. Therefore, each M_m has degree exactly m with a nonzero leading coefficient. For an integer $N \geq 0$, let $\mathcal{P}_N$ denote the space of polynomials of degree at most N. This implies that, when ordered by degree, the set $\{M_0, \ldots, M_N\}$ has an upper-triangular representation in the monomial basis with nonzero diagonal entries and hence is linearly independent. Consequently, $\{M_0, \ldots, M_N\}$ forms a basis of $\mathcal{P}_N$. Thus, since the transformation to the monomial basis is upper-triangular with nonzero diagonal entries:

$$\operatorname{span}\{M_0, \ldots, M_N\} = \mathcal{P}_N. \tag{22}$$

The Mittag-Leffler basis, therefore, has the same approximation space as the monomial basis. Its usefulness here comes from its graded polynomial structure, its recurrence relation, and the possibility of evaluating its fractional integrals analytically after converting it to monomial form. Define:

$$\boldsymbol{M}_N(\theta) = \big[M_0(\theta), \ldots, M_N(\theta)\big]^{\mathsf{T}}. \tag{23}$$

Let $\{(\theta_i^{(b)}, w_i)\}_{i=1}^{n_b}$ be the shifted Gauss-Legendre nodes and positive weights on $[0,1]$ used for basis stabilization, where $n_b \geq N+1$. Form the weighted evaluation matrix $\boldsymbol{A} \in \mathbb{R}^{n_b \times (N+1)}$ by:

$$\boldsymbol{A}_{i,:} = \sqrt{w_i}\,\boldsymbol{M}_N(\theta_i^{(b)})^{\mathsf{T}}, \quad i = 1, \ldots, n_b, \tag{24}$$

and compute its thin QR factorization:

$$\boldsymbol{A} = \boldsymbol{Q}\boldsymbol{R}, \quad \boldsymbol{Q}^{\mathsf{T}}\boldsymbol{Q} = \boldsymbol{I}_{N+1}. \tag{25}$$

The stabilized basis is then defined by:

$$\boldsymbol{\phi}_N(\theta) = \boldsymbol{R}^{-\mathsf{T}}\boldsymbol{M}_N(\theta). \tag{26}$$

Indeed, its weighted evaluation matrix satisfies the following:

$$\sum_{i=1}^{n_b} w_i\,\boldsymbol{\phi}_N(\theta_i^{(b)})\boldsymbol{\phi}_N(\theta_i^{(b)})^{\mathsf{T}} = \boldsymbol{I}_{N+1}. \tag{27}$$

Thus, the transformed functions remain in $\mathcal{P}_N$ and are orthonormal with respect to the discrete weighted inner product induced by the selected quadrature rule, up to floating-point arithmetic errors. For $j = 0, \ldots, N$, write the stabilized basis function in monomial form as:

$$\phi_j(\theta) = \sum_{k=0}^{j} a_{kj}\theta^k. \tag{28}$$

Using the standard identity:

$$I_{0+}^{\beta}\theta^k = \frac{\Gamma(k+1)}{\Gamma(k+\beta+1)}\theta^{k+\beta}, \quad \beta > 0, \tag{29}$$

the fractional integral of ϕ_j can be evaluated analytically as:

$$\big(I_{0+}^{\beta}\phi_j\big)(\theta) = \sum_{k=0}^{j} a_{kj}\frac{\Gamma(k+1)}{\Gamma(k+\beta+1)}\theta^{k+\beta}, \quad \beta>0. \tag{30}$$

Thus, once the basis is expanded in monomial form, no numerical quadrature is required in the evaluation step of applying the fractional integral operator. The expression is algebraically exact, subject only to floating-point errors in the computed coefficients a_{kj}.

3. ψ-Caputo robotic optimal control

3.1. General problem

Let n_z and n_u denote the state and control dimensions, respectively, and let $\mathcal{U}_{\mathrm{ad}} \subset L^2([0,T],\mathbb{R}^{n_u})$ be a nonempty set of admissible controls. Assume that, for every $u \in \mathcal{U}_{\mathrm{ad}}$, the fractional state equation admits a unique solution $z = z[u]$ and that the optimal-control problem below admits at least one optimal pair. Consider the finite-horizon problem:

$$\min_{u\in\mathcal{U}_{\mathrm{ad}}} \mathcal{J}[z,u] = \Phi\big(z(T)\big) + \int_0^T \mathcal{L}\big(t,z(t),u(t)\big)\,dt, \tag{31}$$

subject to:

$${}^{C}D_{0+}^{\alpha,\psi} z(t) = F\big(t,z(t),u(t)\big), \quad z(0)=z_0, \tag{32}$$

where $z(t)\in\mathbb{R}^{n_z}$ and $u(t)\in\mathbb{R}^{n_u}$. Here, $\mathcal{J}$ denotes the performance index, Φ is the terminal cost, $\mathcal{L}$ is the running-cost density, F is the state-dynamics map, and z_0 is the initial state. Define the pullback variables by:

$$\widehat{z}(\theta) = z\big(\chi(\theta)\big), \quad \widehat{u}(\theta) = u\big(\chi(\theta)\big), \tag{33}$$

and the pullback operator:

$$\mathcal{T} : L^2([0,T],\mathbb{R}^{n_u}) \to L^2([0,1],\mathbb{R}^{n_u}), \tag{34}$$

by:

$$(\mathcal{T}u)(\theta) = u(\chi(\theta)). \tag{35}$$

The admissible control set in operational time is therefore defined by $\widehat{\mathcal{U}}_{\mathrm{ad}} = \mathcal{T}(\mathcal{U}_{\mathrm{ad}}) \subset L^2([0,1],\mathbb{R}^{n_u})$. Since $\psi' \in C([0,T])$ and $\psi'(t)>0$ on $[0,T]$, the maps Θ and χ are C^1 bijections, and ψ' is bounded above and below by positive constants on $[0,T]$. Moreover:

$$\begin{aligned}\|\mathcal{T}u\|^2_{L^2([0,1])} &= \int_0^1 \big\|u\big(\chi(\theta)\big)\big\|^2\,d\theta \\ &= \frac{1}{\Delta_\psi}\int_0^T \|u(t)\|^2\,\psi'(t)\,dt \\ &\le \frac{\|\psi'\|_{L^\infty([0,T])}}{\Delta_\psi}\|u\|^2_{L^2([0,T])}.\end{aligned} \tag{36}$$

Therefore, $\mathcal{T}$ is bounded and preserves square integrability. In addition, its inverse is:

$$\big(\mathcal{T}^{-1}\widehat{u}\big)(t) = \widehat{u}\big(\Theta(t)\big). \tag{37}$$

Furthermore:

$$\|\mathcal{T}^{-1}\widehat{u}\|^2_{L^2([0,T])} \le \|\chi'\|_{L^\infty([0,1])}\|\widehat{u}\|^2_{L^2([0,1])}, \tag{38}$$

so $\mathcal{T}$ is a bounded linear operator with bounded inverse $\mathcal{T}^{-1}$ and therefore defines an isomorphism between $L^2([0,T],\mathbb{R}^{n_u})$ and $L^2([0,1],\mathbb{R}^{n_u})$. Hence, admissible physical-time pairs correspond bijectively to admissible operational-time pairs. Consequently, the pullback defines a bijection between admissible pairs, and the physical-time cost functional transforms into its operational-time representation under the change of variables. Finally, the operational-time formulation is:

$$\min_{\widehat{u}\in\widehat{\mathcal{U}}_{\mathrm{ad}}} \Phi\big(\widehat{z}(1)\big) + \int_0^1 \mathcal{L}\big(\chi(\theta),\widehat{z}(\theta),\widehat{u}(\theta)\big)\chi'(\theta)\,d\theta, \tag{39}$$

subject to:

$${}^{C}D_{0+}^{\alpha}\widehat{z}(\theta) = \Delta_\psi^{\alpha} F\big(\chi(\theta),\widehat{z}(\theta),\widehat{u}(\theta)\big), \quad \widehat{z}(0)=z_0, \tag{40}$$

where the scaling factor Δ_ψ^{α} follows directly from the pullback identity in **Theorem 1**. Under the well-posedness assumption stated above, the transformed state equation admits a unique solution for every $\widehat{u}\in\widehat{\mathcal{U}}_{\mathrm{ad}}$. **Equations (39)** and **(40)** show that ψ enters the optimal-control problem as an operational clock through the following four effects:

(1) The lag $\psi(t)-\psi(s)$ and the rate $d\theta/dt = \psi'(t)/\Delta_\psi$ determine how physical time is distributed in the fractional-memory term of the state equation.

(2) The inverse-clock Jacobian $\chi'(\theta)$ determines the physical-time density of the running cost in the operational-time objective.

(3) Since the running cost contains the control-effort density, the physical-time effort associated with an operational control is clock-dependent; for example:

$$\int_0^T \|u(t)\|^2\,dt = \int_0^1 \|\widehat{u}(\theta)\|^2\,\chi'(\theta)d\theta. \tag{41}$$

Therefore, different clocks may lead the optimizer to choose different actuation profiles.

(4) The terminal penalty is evaluated at the same physical endpoint and is not multiplied

by $\chi'(\theta)$. Nevertheless, the terminal state $\widehat{z}(1) = z(T)$ depends on the complete clock-dependent trajectory, so terminal accuracy is also affected by the selected clock.

Thus, ψ is an operational modeling choice that can affect memory distribution, control effort, terminal accuracy, and physical-time cost even when all admissible clocks share the same endpoints.

Remark 2 (Relation to existing methods)**.** *The distinctions between the present framework and fixed-kernel FOCPs, spectral/polynomial discretizations, and fractional LQ formulations are summarized in* ***Table 1****.* ***Equations (39)*** *and* ***(40)*** *provide the corresponding operational-time formulation.*

3.2. Nondimensionalized planar regulator

As a first robotic numerical case, used to demonstrate the exact state-elimination mechanism and the resulting quadratic structure, we consider a two-axis fractional double-integrator surrogate adapted from the vector-valued robotic test problems studied in the recent optimal-control literature.[21] The state and control vectors are:

$$\begin{aligned} z(t) &= \begin{bmatrix} x_1(t) & x_2(t) & v_1(t) & v_2(t) \end{bmatrix}^{\mathsf{T}}, \\ u(t) &= \begin{bmatrix} u_1(t) & u_2(t) \end{bmatrix}^{\mathsf{T}}. \end{aligned} \tag{42}$$

Here, x_i are position-like states, v_i are auxiliary velocity-like states, and u_i are normalized actuation inputs. The ψ-Caputo dynamics are:

$$\begin{cases} {}^{C}D^{\alpha,\psi}_{0+} x_1(t) = v_1(t), & \text{(43a)} \\ {}^{C}D^{\alpha,\psi}_{0+} x_2(t) = v_2(t), & \text{(43b)} \\ {}^{C}D^{\alpha,\psi}_{0+} v_1(t) = u_1(t), & \text{(43c)} \\ {}^{C}D^{\alpha,\psi}_{0+} v_2(t) = u_2(t), & \text{(43d)} \end{cases}$$

with:

$$z(0) = \begin{bmatrix} 1 & -1 & 0 & 0 \end{bmatrix}^{\mathsf{T}}. \tag{44}$$

Also, the physical-time performance index is:

$$\begin{aligned} \mathcal{J}[z,u] &= 25\Big(x_1^2(1) + x_2^2(1)\Big) \\ &\quad + 2\Big(v_1^2(1) + v_2^2(1)\Big) \\ &\quad + \int_0^1 \Big(x_1^2(t) + x_2^2(t) \\ &\qquad + 0.1v_1^2(t) + 0.1v_2^2(t) \\ &\qquad + 0.1u_1^2(t) + 0.1u_2^2(t)\Big)\, dt. \end{aligned} \tag{45}$$

For the clocks used below, $\psi(0) = 0$ and $\psi(1) = 1$, and therefore $\Delta_\psi = \psi(1) - \psi(0) = 1$. Applying **Theorem 1** under its stated regularity assumptions, the robotic dynamics rewritten in operational-time variables via the pullback transformation are:

$$\begin{aligned} {}^{C}D^{\alpha}_{0+} \widehat{x}_1(\theta) &= \widehat{v}_1(\theta), & \text{(46a)} \\ {}^{C}D^{\alpha}_{0+} \widehat{x}_2(\theta) &= \widehat{v}_2(\theta), & \text{(46b)} \\ {}^{C}D^{\alpha}_{0+} \widehat{v}_1(\theta) &= \widehat{u}_1(\theta), & \text{(46c)} \\ {}^{C}D^{\alpha}_{0+} \widehat{v}_2(\theta) &= \widehat{u}_2(\theta). & \text{(46d)} \end{aligned}$$

Since $\widehat{z}(\theta) = z(\chi(\theta))$ and $\chi(0) = 0$, the initial condition is preserved:

$$\widehat{z}(0) = z(0) = \begin{bmatrix} 1 & -1 & 0 & 0 \end{bmatrix}^{\mathsf{T}}. \tag{47}$$

Using the change of variables $t = \chi(\theta)$, with $dt = \chi'(\theta)\, d\theta$, the physical-time cost expressed in operational coordinates is:

$$\begin{aligned} \mathcal{J}[\widehat{z},\widehat{u}] &= 25\Big(\widehat{x}_1^2(1) + \widehat{x}_2^2(1)\Big) \\ &\quad + 2\Big(\widehat{v}_1^2(1) + \widehat{v}_2^2(1)\Big) \\ &\quad + \int_0^1 \Big(\widehat{x}_1^2(\theta) + \widehat{x}_2^2(\theta) \\ &\qquad + 0.1\widehat{v}_1^2(\theta) + 0.1\widehat{v}_2^2(\theta) \\ &\qquad + 0.1\widehat{u}_1^2(\theta) + 0.1\widehat{u}_2^2(\theta)\Big)\chi'(\theta)\, d\theta. \end{aligned} \tag{48}$$

Each clock used in the simulations belongs to $C^1([0,1])$ and satisfies $\psi'(t) > 0$ on $[0,1]$. Since ψ' is continuous and strictly positive on the compact interval, ψ is a C^1 diffeomorphism between $[0,1]$ and its image, and ψ' is bounded above and below by positive constants, which ensures a well-defined and bounded inverse mapping χ'. Thus, there exist constants $m_\psi, M_\psi > 0$ such that:

$$0 < m_\psi \le \psi'(t) \le M_\psi < \infty, \quad t \in [0,1]. \tag{49}$$

Consequently:

$$\chi'(\theta) = \frac{\Delta_\psi}{\psi'(\chi(\theta))}, \tag{50}$$

is positive and bounded on $[0,1]$. The clocks are normalized as follows:

$$\psi(0) = 0, \quad \psi(1) = 1, \tag{51}$$

and hence $\Delta_\psi = 1$. Therefore, the ψ-Caputo scaling factor in **Theorem 1** becomes unity in operational time. The selected clocks are:

$$\psi_{\mathrm{id}}(t) = t, \tag{52}$$

$$\psi_{\log}(t) = \frac{\log(1+4t)}{\log 5}, \tag{53}$$

$$\psi_{\mathrm{pow}}(t) = \frac{(1+t)^2 - 1}{3}, \tag{54}$$

$$\psi_{\exp}(t) = \frac{e^{2t} - 1}{e^2 - 1}. \tag{55}$$

Their inverse maps and Jacobians are given in **Table 2**. **Figure 1** illustrates both the clocks and the induced weights. As can be seen, all clocks

share the same endpoints but allocate physical time differently over θ. The local rate $\psi'(t)$ determines how rapidly the operational memory clock advances relative to physical time, whereas $\chi'(\theta)$ determines the physical-time density appearing in the running cost after the pullback. Hence, the selected clock changes both the memory distribution and the cost density used by the optimizer. This is why the clock can modify the required control effort, the achieved terminal accuracy, and the total physical-time objective even when $\Delta_\psi = 1$.

Table 2. Normalized clocks used in the simulations

Clock	$t = \chi(\theta)$	$\chi'(\theta)$
Identity	θ	1
Logarithmic	$\dfrac{5^\theta - 1}{4}$	$\dfrac{(\log 5)\,5^\theta}{4}$
Power	$\sqrt{1+3\theta} - 1$	$\dfrac{3}{2\sqrt{1+3\theta}}$
Exponential	$\dfrac{1}{2}\log\big(1 + (e^2-1)\theta\big)$	$\dfrac{e^2-1}{2\big(1+(e^2-1)\theta\big)}$

3.3. Nonlinear two-link manipulator model

To address robotic dynamics beyond the linear regulator benchmark, we also consider a standard two-link planar manipulator in joint coordinates.[37] Let:

$$q(t) = \begin{bmatrix} q_1(t) \\ q_2(t) \end{bmatrix}, \quad \omega(t) = \begin{bmatrix} \omega_1(t) \\ \omega_2(t) \end{bmatrix}, \quad \tau(t) = \begin{bmatrix} \tau_1(t) \\ \tau_2(t) \end{bmatrix}. \tag{56}$$

Here, q_i are joint angles, ω_i are velocity-like states, and τ_i are actuator torques. The ψ-Caputo fractional manipulator model is written as:

$$\begin{aligned} {}^{C}D^{\alpha,\psi}_{0+} q(t) &= \omega(t), \\ {}^{C}D^{\alpha,\psi}_{0+} \omega(t) &= M(q(t))^{-1}\Big[\tau(t) - C(q(t),\omega(t))\omega(t) \\ &\quad - G(q(t)) - D\omega(t)\Big]. \end{aligned} \tag{57}$$

Here, $M(q)$ is the inertia matrix, $C(q,\omega)\omega$ is the Coriolis/centrifugal vector, $G(q)$ is the gravity vector, and $D = \mathrm{diag}(b_1, b_2)$ is the viscous-damping matrix. For $i = 1, 2$, m_i denotes the link mass, l_i the link length, l_{ci} the distance to the link center of mass, I_i the link moment of inertia, and b_i the viscous-damping coefficient; g_0 denotes gravitational acceleration. The inertia matrix is:

$$M(q) = \begin{bmatrix} M_{11} & M_{12} \\ M_{12} & M_{22} \end{bmatrix}, \tag{58}$$

where:

$$\begin{aligned} M_{11} &= I_1 + I_2 + m_1 l_{c1}^2 \\ &\quad + m_2\big(l_1^2 + l_{c2}^2 + 2 l_1 l_{c2}\cos q_2\big), \\ M_{12} &= I_2 + m_2\big(l_{c2}^2 + l_1 l_{c2}\cos q_2\big), \\ M_{22} &= I_2 + m_2 l_{c2}^2. \end{aligned} \tag{59}$$

The Coriolis/centrifugal vector and gravity vector are:

$$C(q,\omega)\omega = \begin{bmatrix} -m_2 l_1 l_{c2}\sin q_2\,(2\omega_1\omega_2 + \omega_2^2) \\ m_2 l_1 l_{c2}\sin q_2\,\omega_1^2 \end{bmatrix}, \tag{60}$$

$$\begin{aligned} G(q) &= \begin{bmatrix} G_1(q) \\ G_2(q) \end{bmatrix}, \\ G_1(q) &= (m_1 l_{c1} + m_2 l_1) g_0 \cos q_1 \\ &\quad + m_2 l_{c2} g_0 \cos(q_1 + q_2), \\ G_2(q) &= m_2 l_{c2} g_0 \cos(q_1 + q_2). \end{aligned} \tag{61}$$

The nonlinear validation uses the parameter values:

$$\begin{aligned} &m_1 = m_2 = 1, \quad l_1 = l_2 = 1, \quad l_{c1} = l_{c2} = 0.5, \\ &I_1 = I_2 = \frac{1}{12}, \quad g_0 = 9.81, \qquad b_1 = b_2 = 0.05, \end{aligned} \tag{62}$$

with $q(0) = [0,0]^\mathsf{T}$, $\omega(0) = [0,0]^\mathsf{T}$, and target joint vector $q_f = [\pi/3, -\pi/4]^\mathsf{T}$. For the end-effector plots, the Cartesian position is computed from the standard planar forward kinematics:

$$p(q) = \begin{bmatrix} l_1\cos q_1 + l_2\cos(q_1+q_2) \\ l_1\sin q_1 + l_2\sin(q_1+q_2) \end{bmatrix}. \tag{63}$$

The performance index for this case is:

$$\begin{aligned} J_m &= 120\,\|q(1) - q_f\|_2^2 + 10\,\|\omega(1)\|_2^2 \\ &\quad + \int_0^1 \Big[20\,\|q(t) - q_f\|_2^2 + \|\omega(t)\|_2^2 \\ &\quad + 0.01\,\|\tau(t)\|_2^2\Big] dt. \end{aligned} \tag{64}$$

For the normalized clocks in **Equations (52)–(55)**, $\Delta_\psi = 1$; hence, the operational-time form of **Equation (57)** has the same Caputo order in θ, while the running part of **Equation (64)** is multiplied by $\chi'(\theta)$ according to **Equation (15)**.

4. Mittag-Leffler reduced-space discretization

4.1. Control approximation and exact state elimination

For the normalized clocks considered here, we have $\Delta_\psi = 1$, so the operational-time dynamics in **Equation (46)** do not include the scaling factor Δ_ψ^α. For each axis, write:

$$\widehat{u}_N(\theta) = \boldsymbol{\phi}_N(\theta)^\mathsf{T} c, \tag{65}$$

where $c \in \mathbb{R}^{N+1}$ is the polynomial coefficient vector. In the regulator used here, no pointwise state

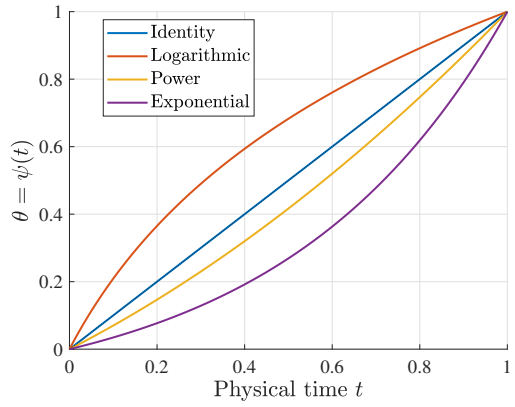
or control constraints are imposed. Consequently, the reduced coefficient problem is unconstrained over $\mathbb{R}^{N+1}$. For the polynomial control approximation, the resulting functions are absolutely continuous on $[0,1]$, so the Caputo derivatives and Riemann-Liouville fractional integrals used below are well-defined. The standard identities are:

$$ {}^{C}D^{\alpha}_{0+} I^{\alpha}_{0+} w = w, \quad I^{\alpha}_{0+} {}^{C}D^{\alpha}_{0+} y = y - y(0), \tag{66}$$

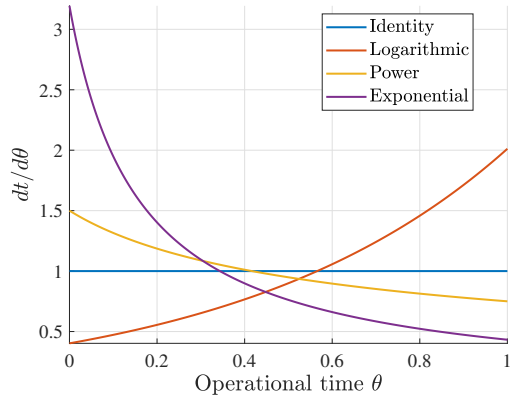
for functions $w, y \in AC([0,1])$ satisfying the usual initial-value compatibility conditions. In the regulator, the initial condition in **Equation (44)** gives $v_1(0) = v_2(0) = 0$. For either axis, $x_0 = x(0)$ denotes its initial position. Applying I^{α}_{0+} componentwise to the operational-time state equations, using **Equation (66)** and linearity, yields:

$$ \widehat{v}_N(\theta) = I^{\alpha}_{0+} \widehat{u}_N(\theta) = \boldsymbol{f}_{\alpha}(\theta)^{\mathsf{T}} c, \tag{67}$$

$$ \widehat{x}_N(\theta) = x_0 + I^{\alpha}_{0+} \widehat{v}_N(\theta) = x_0 + \boldsymbol{f}_{2\alpha}(\theta)^{\mathsf{T}} c. \tag{68}$$



(a) Four admissible normalized clocks $\theta = \psi(t)$



(b) Corresponding inverse-clock Jacobians $\chi'(\theta) = dt/d\theta$

Figure 1. Normalized operational-clock mappings and their induced physical-time densities

The above relations follow from the analytically exact evaluation of $I^{\beta}_{0+}\phi_j$ in **Equation (30)**, together with the representation of each basis function in monomial form. For $j = 0, \ldots, N$, the jth component of $\boldsymbol{f}_{\beta}(\theta)$ is $I^{\beta}_{0+}\phi_j(\theta)$, evaluated by **Equation (30)**. Consequently, within the constructed polynomial approximation and in the sense of the imposed reconstruction identities, we have the following:

$$ {}^{C}D^{\alpha}_{0+} \widehat{v}_N = \widehat{u}_N, \quad {}^{C}D^{\alpha}_{0+} \widehat{x}_N = \widehat{v}_N. \tag{69}$$

Let $\{\theta_i, \varpi_i\}_{i=1}^{n_q}$ be the shifted Gauss-Legendre nodes and weights on $[0,1]$, with $n_q \geq N+1$. Define the physical-time quadrature weights by:

$$ \widetilde{\varpi}_i = \varpi_i \chi'(\theta_i), \quad i = 1, \ldots, n_q. \tag{70}$$

Since $\varpi_i > 0$ and $\chi'(\theta_i) > 0$, it follows that all $\widetilde{\varpi}_i$ are strictly positive. The condition $n_q \geq N+1$ is used below to guarantee that the control evaluation matrix has full column rank. Define $\boldsymbol{B}, \boldsymbol{F}_{\alpha}, \boldsymbol{F}_{2\alpha} \in \mathbb{R}^{n_q \times (N+1)}$ by:

$$ \begin{aligned} (\boldsymbol{B})_{i,:} &= \boldsymbol{\phi}_N(\theta_i)^{\mathsf{T}}, \quad \boldsymbol{B} \in \mathbb{R}^{n_q \times (N+1)}, \\ (\boldsymbol{F}_{\beta})_{i,:} &= \boldsymbol{f}_{\beta}(\theta_i)^{\mathsf{T}}, \quad \beta \in \{\alpha, 2\alpha\}, \end{aligned} \tag{71}$$

and set:

$$ \begin{aligned} W &= \operatorname{diag}\left(\widetilde{\varpi}_1, \ldots, \widetilde{\varpi}_{n_q}\right), \\ \mathbf{1}_{n_q} &= \begin{bmatrix} 1 & \cdots & 1 \end{bmatrix}^{\mathsf{T}}. \end{aligned} \tag{72}$$

Thus, $W \in \mathbb{R}^{n_q \times n_q}$ is symmetric positive definite. For one axis, the Gauss-Legendre approximation of the physical-time cost yields a quadratic functional in c of the form:

$$ J_{N,n_q}(c) = c^{\mathsf{T}} H c + 2 g^{\mathsf{T}} c + \kappa, \tag{73}$$

where H is symmetric by construction since each term is a quadratic form induced by symmetric quadrature weights and inner-product (Gram-type) structures:

$$ \begin{aligned} H = {} & q_x \boldsymbol{F}_{2\alpha}^{\mathsf{T}} W \boldsymbol{F}_{2\alpha} + q_v \boldsymbol{F}_{\alpha}^{\mathsf{T}} W \boldsymbol{F}_{\alpha} + r \boldsymbol{B}^{\mathsf{T}} W \boldsymbol{B} \\ & + s_x \boldsymbol{f}_{2\alpha}(1) \boldsymbol{f}_{2\alpha}(1)^{\mathsf{T}} + s_v \boldsymbol{f}_{\alpha}(1) \boldsymbol{f}_{\alpha}(1)^{\mathsf{T}}, \end{aligned} \tag{74}$$

$$ g = q_x x_0 \boldsymbol{F}_{2\alpha}^{\mathsf{T}} W \mathbf{1}_{n_q} + s_x x_0 \boldsymbol{f}_{2\alpha}(1), \tag{75}$$

$$ \kappa = q_x x_0^2 \mathbf{1}_{n_q}^{\mathsf{T}} W \mathbf{1}_{n_q} + s_x x_0^2. \tag{76}$$

Here, q_x, q_v, r, s_x, and s_v denote the running position, running velocity, running control, terminal position, and terminal velocity weights, respectively. In this context, the weights are chosen as $q_x = 1$, $q_v = 0.1$, $r = 0.1$, $s_x = 25$, and $s_v = 2$.

Proposition 1 (Unique discrete minimizer)**.** *Assume that:*

$$ q_x, q_v, s_x, s_v \geq 0, \quad r > 0, \tag{77}$$

*that the physical-time quadrature weights satisfy $\widetilde{\varpi}_i > 0$, and that $n_q \geq N+1$. Then, the matrix H in **Equation (74)** is symmetric positive definite. Consequently, J_{N,n_q} is strictly convex on $\mathbb{R}^{N+1}$ and has a unique minimizer c^*, characterized as the unique solution of:*

$$ H c^* = -g. \tag{78}$$

Proof. Each term in **Equation (74)** is symmetric positive semidefinite. Hence, for any nonzero

$y \in \mathbb{R}^{N+1}$:

$$y^{\mathsf{T}} H y \geq r\,(\boldsymbol{B}y)^{\mathsf{T}} W (\boldsymbol{B}y). \tag{79}$$

To establish positive definiteness, it remains to show that $\boldsymbol{B}$ has full column rank. Define:

$$p_y(\theta) = \boldsymbol{\phi}_N(\theta)^{\mathsf{T}} y. \tag{80}$$

Because $\{\phi_0, \ldots, \phi_N\}$ is a basis of $\mathcal{P}_N$, the function p_y is a nonzero polynomial of degree at most N whenever $y \neq 0$. If $\boldsymbol{B}y = 0$, then:

$$p_y(\theta_i) = 0, \quad i = 1, \ldots, n_q. \tag{81}$$

Thus, p_y would have at least $n_q \geq N+1$ distinct zeros in $[0,1]$. Since a nonzero polynomial of degree at most N cannot have more than N distinct roots in $[0,1]$, this implies that p_y must be identically zero, i.e., $p_y \equiv 0$, which contradicts the assumption $y \neq 0$. Therefore, the mapping $y \mapsto p_y$ is injective. Moreover, since $W \succ 0$, $r > 0$, and $\boldsymbol{B}$ has full column rank, it follows that:

$$r\,(\boldsymbol{B}y)^{\mathsf{T}} W (\boldsymbol{B}y) > 0, \tag{82}$$

for every nonzero $y \in \mathbb{R}^{N+1}$. Consequently:

$$y^{\mathsf{T}} H y > 0, \quad y \neq 0, \tag{83}$$

which implies that H is symmetric positive definite. □

Let c_+^* denote the optimal coefficient vector for the first axis, where $x_0 = 1$. Because the two axes are dynamically decoupled and use the same fractional order, clock, cost weights, basis, and quadrature rule, they have the same matrix H. Moreover, **Equation (75)** shows that g depends linearly on x_0. Hence, for the second axis, where $x_0 = -1$:

$$g_- = -g_+. \tag{84}$$

For the first axis, **Equation (78)** gives:

$$H c_+^* = -g_+. \tag{85}$$

Therefore:

$$H(-c_+^*) = g_+ = -g_-. \tag{86}$$

By the uniqueness of the solution of the second-axis linear system, it follows that:

$$c_-^* = -c_+^*. \tag{87}$$

The constant term κ is identical for the two axes because it depends on x_0^2. Therefore, the complete two-axis solution is recovered from one linear solve of size $N+1$, followed by a sign reversal for the second axis.

4.2. Algorithmic workflow

For the linear planar regulator, the reduced-space procedure is summarized below:

(1) Select the fractional order α, an admissible normalized clock ψ, the polynomial degree N, a basis-construction quadrature order $n_b \geq N+1$, and an initial cost quadrature order $n_q \geq N+1$.
(2) Generate $M_0, \ldots, M_N$ from **Equations (18)** and **(19)** in ascending power-coefficient form.
(3) Form the weighted evaluation matrix $\boldsymbol{A}$, compute its thin QR factorization $\boldsymbol{A} = \boldsymbol{Q}\boldsymbol{R}$, and construct the stabilized basis from **Equation (26)**.
(4) Convert the stabilized basis functions to monomial form and evaluate $\boldsymbol{B}$, $\boldsymbol{F}_\alpha$, and $\boldsymbol{F}_{2\alpha}$ using **Equation (30)**.
(5) Evaluate $\chi'(\theta_i)$ and construct the positive physical-time weights and the matrix W from **Equations (70)** and **(72)**.
(6) Assemble H, g, and κ from **Equations (74)**–**(76)**. Then, solve the symmetric positive-definite system:
$$H c^* = -g, \tag{88}$$
using a numerically stable solver, preferably a Cholesky factorization.
(7) Reconstruct the first-axis control and states from **Equations (65)**, **(67)**, and **(68)**, and obtain the second-axis quantities by the sign symmetry $c_-^* = -c_+^*$.
(8) Compute J_{N,n_q}, the terminal-state norm, physical-time control energy, peak control, condition number, and the algebraic optimality residual $\|Hc^* + g\|_2$.

The computational cost of the linear reduced-space algorithm can be expressed in terms of the polynomial dimension $N+1$, the basis-construction quadrature order n_b, and the cost quadrature order n_q. Forming the $n_b \times (N+1)$ weighted evaluation matrix and computing its thin QR factorization requires $O(n_b(N+1)^2)$ operations. Evaluation of the stabilized basis and its analytical fractional integrals at the n_q quadrature points, together with assembly of the Gram-type terms in H and g, requires $O(n_q(N+1)^2)$ operations. The remaining dense $(N+1) \times (N+1)$ transformations and the Cholesky solution of the symmetric positive-definite reduced system require $O((N+1)^3)$ operations. Hence, the overall arithmetic complexity of the linear reduced-space computation for a given fractional order and clock is:

$$O\big((n_b + n_q)(N+1)^2 + (N+1)^3\big). \tag{89}$$

Since $n_b, n_q \geq N+1$, this may also be written asymptotically as $O((n_b + n_q)(N+1)^2)$. The two-axis regulator requires only one reduced linear solve because the second-axis coefficients follow

from the symmetry $c_-^* = -c_+^*$. For the nonlinear direct-collocation formulation, the total optimization cost also depends on the number of nonlinear-programming iterations and the linear-algebra strategy used by the NLP solver.

4.3. Direct collocation form for nonlinear robotic dynamics

For nonlinear dynamics such as **Equation (57)**, complete state elimination is generally not available because the acceleration equation depends nonlinearly on the state. For the normalized clocks used here, $\Delta_\psi = 1$, and $q_0 = q(0)$ and $\omega_0 = \omega(0) = 0$ denote the initial joint and velocity-like states. Let $\widehat{r}_{\omega,N}$ approximate the Caputo derivative of the velocity-like state and let $\widehat{\tau}_N$ denote the torque approximation:

$$\begin{aligned} \widehat{r}_{\omega,N}(\theta) &= A_\omega^{\mathsf{T}} \boldsymbol{\phi}_N(\theta), \\ \widehat{\tau}_N(\theta) &= C_\tau^{\mathsf{T}} \boldsymbol{\phi}_N(\theta), \end{aligned} \tag{90}$$

where $A_\omega, C_\tau \in \mathbb{R}^{(N+1)\times 2}$ are the corresponding coefficient matrices. The states are reconstructed as:

$$\begin{aligned} \widehat{\omega}_N(\theta) &= I_{0+}^{\alpha} \widehat{r}_{\omega,N}(\theta), \\ \widehat{q}_N(\theta) &= q_0 + I_{0+}^{2\alpha} \widehat{r}_{\omega,N}(\theta). \end{aligned} \tag{91}$$

By the fractional-integral semigroup property, this reconstruction satisfies:

$${}^{C}D_{0+}^{\alpha} \widehat{q}_N(\theta) = \widehat{\omega}_N(\theta), \tag{92}$$

by construction. Therefore, only the nonlinear acceleration equation is imposed at the collocation nodes $\{\theta_j\}_{j=1}^{n_c}$, where n_c is the number of collocation nodes:

$$\widehat{r}_{\omega,N}(\theta_j) - f_m\big(\widehat{q}_N(\theta_j), \widehat{\omega}_N(\theta_j), \widehat{\tau}_N(\theta_j)\big) = 0, \tag{93}$$

for $j = 1, \dots, n_c$. Here, $f_m(q, \omega, \tau)$ denotes the acceleration right-hand side in the second line of **Equation (57)**. The physical-time cost is approximated by the same Jacobian-weighted Gauss-Legendre rule used in **Equation (70)**. The resulting finite-dimensional problem is nonlinear and is solved using sequential quadratic programming.

5. Approximation properties and numerical reliability

5.1. Consistency and polynomial exactness

Because $\operatorname{span}\{M_0, \dots, M_N\} = \mathcal{P}_N$, the stabilized basis in **Equation (26)** spans the same polynomial space. For any control approximation $\widehat{u}_N = \boldsymbol{\phi}_N^{\mathsf{T}} c \in \mathcal{P}_N$, linearity of the fractional integral and the semigroup property give the following:

$$\widehat{v}_N = I_{0+}^{\alpha} \widehat{u}_N = \boldsymbol{f}_\alpha^{\mathsf{T}} c, \quad \widehat{x}_N = x_0 + I_{0+}^{\alpha} \widehat{v}_N. \tag{94}$$

Furthermore, using the semigroup property of the Riemann-Liouville fractional integral, we obtain:

$$I_{0+}^{\alpha} \widehat{v}_N = I_{0+}^{2\alpha} \widehat{u}_N, \tag{95}$$

which yields:

$$\widehat{x}_N = x_0 + \boldsymbol{f}_{2\alpha}^{\mathsf{T}} c. \tag{96}$$

Although the fractional integral of a polynomial is generally not a polynomial when the integration order is noninteger, **Equation (30)** evaluates each fractional-integral basis function analytically as a finite sum of generalized powers. Consequently, the reconstructed states are evaluated in closed analytical form in terms of generalized power functions $\theta^{k+\beta}$, with numerical error arising from floating-point evaluation, coefficient transformation, and basis construction; in contrast, approximation error is governed separately by the polynomial truncation in $\mathcal{P}_N$. Objective quadrature is a separate approximation and does not affect the algebraic exactness of the state reconstruction. If the exact continuous minimizer belongs to $\mathcal{P}_N$, then the exactly integrated polynomially restricted problem recovers that minimizer. Define the weighted inner product and norm by:

$$\begin{aligned} \langle f, g \rangle_{\chi'} &= \int_0^1 f(\theta) g(\theta) \chi'(\theta)\, d\theta, \\ \|f\|_{L^2_{\chi'}}^2 &= \langle f, f \rangle_{\chi'}. \end{aligned} \tag{97}$$

Theorem 2 (Convergence in the robot regulator)**.** *Assume that:*

$$\begin{aligned} &\frac{1}{2} < \alpha \le 1, \\ &0 < m_\chi \le \chi'(\theta) \le M_\chi < \infty, \quad \theta \in [0,1], \end{aligned} \tag{98}$$

and that $r > 0$, while $q_x, q_v, s_x, s_v \ge 0$. Then, the exact continuous one-axis functional J possesses a unique minimizer u^* over $L^2_{\chi'}(0,1)$. Moreover, for every $N \ge 0$, the restriction of J to $\mathcal{P}_N$ possesses a unique minimizer u_N^*. In addition, there exists a constant $C > 0$, independent of N, such that:

$$\|u_N^* - u^*\|_{L^2_{\chi'}} \le C \inf_{p_N \in \mathcal{P}_N} \|u^* - p_N\|_{L^2_{\chi'}}. \tag{99}$$

Consequently:

$$\|u_N^* - u^*\|_{L^2_{\chi'}} \to 0, \quad J(u_N^*) \to J(u^*), \tag{100}$$

as $N \to \infty$. Furthermore, if $u^* \in H^s(0,1)$ for some $s > 0$, then the standard polynomial approximation estimate gives:

$$\|u_N^* - u^*\|_{L^2_{\chi'}} \le C_s N^{-s} \|u^*\|_{H^s(0,1)}, \tag{101}$$

where C_s is independent of N. The corresponding objective error satisfies the following:

$$0 \le J(u_N^*) - J(u^*) \le \widetilde{C}_s N^{-2s} \|u^*\|_{H^s(0,1)}^2. \tag{102}$$

Proof. Let:

$$\mathcal{S}_\beta u := I_{0+}^{\beta} u, \quad \lambda_\beta(u) = \big(\mathcal{S}_\beta u\big)(1). \tag{103}$$

The fractional integral operator $\mathcal{S}_\beta$ is bounded on $L^2(0,1)$ for every $\beta > 0$. This follows from Young's inequality since the kernel $(1-s)^{\beta-1}$ is integrable on $(0,1)$ for all $\beta > 0$. Moreover, for $\beta > \frac{1}{2}$ (to ensure integrability of the kernel square), the Cauchy-Schwarz inequality gives:

$$\begin{aligned} |\lambda_\beta(u)| &= \frac{1}{\Gamma(\beta)} \left| \int_0^1 (1-s)^{\beta-1} u(s)\, ds \right| \\ &\leq \frac{1}{\Gamma(\beta)\sqrt{2\beta-1}} \|u\|_{L^2(0,1)}. \end{aligned} \tag{104}$$

Hence, because $\alpha > \frac{1}{2}$, both λ_α and $\lambda_{2\alpha}$ are bounded linear functionals on $L^2(0,1)$. The assumed upper and lower bounds on χ' imply that the weighted norm in **Equation (97)** is equivalent to the ordinary $L^2(0,1)$ norm. The quadratic part of the exact one-axis functional defines the symmetric bilinear form:

$$\begin{aligned} a(u,w) =& q_x \langle \mathcal{S}_{2\alpha} u, \mathcal{S}_{2\alpha} w \rangle_{\chi'} + q_v \langle \mathcal{S}_\alpha u, \mathcal{S}_\alpha w \rangle_{\chi'} \\ &+ r \langle u, w \rangle_{\chi'} + s_x \lambda_{2\alpha}(u) \lambda_{2\alpha}(w) \\ &+ s_v \lambda_\alpha(u) \lambda_\alpha(w). \end{aligned} \tag{105}$$

This bilinear form is continuous on $L^2_{\chi'}(0,1)$. Furthermore, because all terms in $a(u,u)$ other than the control-penalty term are nonnegative:

$$a(u,u) \geq r \|u\|^2_{L^2_{\chi'}}. \tag{106}$$

Therefore, a is coercive on $L^2_{\chi'}(0,1)$ with coercivity constant $r > 0$. The terms depending linearly on the control define the bounded linear functional:

$$\ell(w) = q_x x_0 \langle 1, \mathcal{S}_{2\alpha} w \rangle_{\chi'} + s_x x_0 \lambda_{2\alpha}(w). \tag{107}$$

The exact one-axis functional can therefore be written as:

$$J(u) = a(u,u) + 2\ell(u) + \kappa, \tag{108}$$

where κ is a constant independent of u, provided that the involved functions satisfy the standard Caputo-Riemann-Liouville compatibility conditions. Since a is continuous and coercive on $L^2_{\chi'}(0,1)$ and ℓ is continuous, the Lax-Milgram theorem yields a unique $u^* \in L^2_{\chi'}(0,1)$ satisfying:

$$a(u^*, w) + \ell(w) = 0, \quad \forall\, w \in L^2_{\chi'}(0,1). \tag{109}$$

This function is the unique minimizer of J. Similarly, coercivity of the restriction of a to the finite-dimensional space $\mathcal{P}_N$ yields a unique minimizer $u_N^* \in \mathcal{P}_N$ satisfying:

$$a(u_N^*, p_N) + \ell(p_N) = 0, \quad \forall\, p_N \in \mathcal{P}_N. \tag{110}$$

Subtracting these relations gives the Galerkin orthogonality condition:

$$a(u^* - u_N^*, p_N) = 0, \quad p_N \in \mathcal{P}_N. \tag{111}$$

Let $e_N = u^* - u_N^*$. For any $p_N \in \mathcal{P}_N$, **Equations (106)** and **(111)** imply:

$$\begin{aligned} r \|e_N\|^2_{L^2_{\chi'}} &\leq a(e_N, e_N) \\ &= a(e_N, u^* - p_N) \\ &\leq C_a \|e_N\|_{L^2_{\chi'}} \|u^* - p_N\|_{L^2_{\chi'}}, \end{aligned} \tag{112}$$

where C_a is the continuity constant of a. Therefore:

$$\|u_N^* - u^*\|_{L^2_{\chi'}} \leq \frac{C_a}{r} \inf_{p_N \in \mathcal{P}_N} \|u^* - p_N\|_{L^2_{\chi'}}. \tag{113}$$

Since $0 < m_\chi \leq \chi'(\theta) \leq M_\chi < \infty$ and χ' is strictly positive and bounded, the norms $\|\cdot\|_{L^2(0,1)}$ and $\|\cdot\|_{L^2_{\chi'}}$ are equivalent. Therefore, density of $\mathcal{P}_N$ in $L^2(0,1)$ implies density in $L^2_{\chi'}(0,1)$:

$$\inf_{p_N \in \mathcal{P}_N} \|u^* - p_N\|_{L^2_{\chi'}} \to 0. \tag{114}$$

The quasi-optimality estimate then gives:

$$\|u_N^* - u^*\|_{L^2_{\chi'}} \to 0. \tag{115}$$

Furthermore, because $J(u) = a(u,u) + 2\ell(u) + \kappa$ and $a(u^*, w) + \ell(w) = 0$ for every $w \in L^2_{\chi'}(0,1)$, the objective error satisfies:

$$J(u_N^*) - J(u^*) = a(u_N^* - u^*, u_N^* - u^*). \tag{116}$$

Consequently:

$$0 \leq J(u_N^*) - J(u^*) \leq C_a \|u_N^* - u^*\|^2_{L^2_{\chi'}}, \tag{117}$$

and since $\|u_N^* - u^*\|_{L^2_{\chi'}} \to 0$, we conclude:

$$J(u_N^*) \to J(u^*). \tag{118}$$

If $u^* \in H^s(0,1)$, the standard best-polynomial approximation estimate gives the following:

$$\inf_{p_N \in \mathcal{P}_N} \|u^* - p_N\|_{L^2_{\chi'}} \leq C_{\text{app}} N^{-s} \|u^*\|_{H^s(0,1)}. \tag{119}$$

Combining this estimate with quasi-optimality and **Equation (116)** proves both the control-error and objective-error estimates stated in the theorem. □

The restriction $\alpha > \frac{1}{2}$ in **Theorem 2** is associated with the continuous L^2 convergence analysis rather than with the construction of the finite-dimensional approximation itself. In the regulator, the terminal velocity-like state contains the endpoint quantity $\lambda_\alpha(u) = (\mathcal{S}_\alpha u)(1)$. The condition $\alpha > \frac{1}{2}$ ensures, through **Equation (104)**, that this endpoint evaluation is a bounded linear functional of an L^2 control, so that the terminal terms in the quadratic functional are continuous in the space used in the proof. For $0 < \alpha \leq \frac{1}{2}$, this boundedness is not guaranteed for arbitrary L^2

controls, and therefore **Theorem 2** does not directly apply without additional regularity assumptions or a different functional setting. The polynomial discretization itself remains well-defined because the approximating controls are smooth finite-dimensional functions. In the numerical experiments considered in this work, all tested fractional orders satisfy $\alpha > \frac{1}{2}$.

Theorem 2 concerns the exact functional restricted to the polynomial space $\mathcal{P}_N$, whereas the coefficient vector computed in Section 4 minimizes the quadrature-based functional J_{N,n_q}. For fixed N, let H_N and g_N denote the Hessian and linear vector obtained by exact integration, and let H_{N,n_q} and g_{N,n_q} denote their Gauss-Legendre approximations. Define:

$$c_N^* = -H_N^{-1} g_N, \quad c_{N,n_q}^* = -H_{N,n_q}^{-1} g_{N,n_q}. \quad (120)$$

For fixed N, each function $\mathcal{S}_\beta \phi_j$ is a finite sum of generalized powers $\theta^{k+\beta}$ and is therefore continuous on $[0,1]$. Since χ' is also continuous and bounded, every integrand entering H_N and g_N is continuous on $[0,1]$. Since all integrands entering H_N and g_N are continuous on $[0,1]$, and the Gauss-Legendre rule is convergent for continuous functions, it implies entrywise convergence of all matrix and vector components:

$$\|H_{N,n_q} - H_N\|_2 \to 0, \quad \|g_{N,n_q} - g_N\|_2 \to 0, \quad (121)$$

as $n_q \to \infty$. Hence, for sufficiently large n_q, we have:

$$\lambda_{\min}(H_{N,n_q}) > 0, \quad (122)$$

so H_{N,n_q} remains symmetric positive definite and invertible. Consequently, since $\lambda_{\min}(H_{N,n_q})$ is bounded away from zero for sufficiently large n_q, the sequence H_{N,n_q}^{-1} is uniformly bounded in operator norm. Using the perturbation identity:

$$H_{N,n_q}^{-1} - H_N^{-1} = H_{N,n_q}^{-1}(H_N - H_{N,n_q})H_N^{-1}, \quad (123)$$

we obtain:

$$\begin{aligned} &\|H_{N,n_q}^{-1} - H_N^{-1}\|_2 \\ &\le \|H_{N,n_q}^{-1}\|_2 \|H_N - H_{N,n_q}\|_2 \|H_N^{-1}\|_2 \to 0. \end{aligned} \quad (124)$$

Since $H_{N,n_q} \to H_N$ and $H_N \succ 0$, the matrices H_{N,n_q}^{-1} are uniformly bounded for sufficiently large n_q. Therefore:

$$H_{N,n_q}^{-1} \to H_N^{-1}. \quad (125)$$

Consequently:

$$c_{N,n_q}^* \to c_N^*, \quad n_q \to \infty. \quad (126)$$

Thus, convergence of the fully discrete method requires both polynomial-space refinement and sufficiently accurate quadrature. The condition $n_q \ge N+1$ guarantees full column rank of the control evaluation matrix and hence positive definiteness of the discrete Hessian, but it does not by itself constitute a quadrature-accuracy criterion. In practice, the adequacy of n_q should be verified by repeating the calculation with an increased quadrature order and monitoring the changes in the objective, coefficient vector, and terminal quantities.

5.2. Conditioning

The recurrence in **Equation (19)** produces polynomials whose leading coefficients grow as 2^m, and the magnitudes of other power coefficients may also increase with degree. Direct computation in the resulting raw basis can therefore amplify coefficient scaling and floating-point errors. The QR transformation leaves the approximation space $\mathcal{P}_N$ unchanged and, in exact arithmetic, represents the same discrete control and state functions in different coordinates. In floating-point arithmetic, it purpose is to provide better-scaled coefficient coordinates through discrete orthonormalization. The spectral condition number $\kappa_2(H)$ depends on the chosen discrete representation; it should be interpreted as a property of the finite-dimensional discretized system rather than the underlying continuous optimal-control operator. Because the reduced coefficient problem is unconstrained, its Karush-Kuhn-Tucker (KKT) condition reduces to the stationarity equation:

$$Hc^* + g = 0. \quad (127)$$

The stationarity residual norm monitors the algebraic solution accuracy:

$$r_{\mathrm{KKT}} = \|Hc^* + g\|_2. \quad (128)$$

Values of order 10^{-15} or smaller indicate that the assembled stationarity equation is satisfied to approximately double-precision accuracy. This residual does not measure polynomial truncation error, objective-quadrature error, model error, or physical validity of the selected kernel; it verifies the numerical solution of the discrete algebraic optimality equation.

6. Simulation and comparison results

6.1. Computational setting

All simulations use $T = 1$, $n_q = 220$ shifted Gauss-Legendre nodes for assembling the cost matrices, and $n_b = 240$ shifted Gauss-Legendre nodes for the QR basis stabilization. Unless stated otherwise, the linear regulator computations use $N = 8$. The nonlinear two-link manipulator validation uses $N = 13$ and $n_c = N + 1 = 14$ collocation nodes, with a sequential quadratic programming implementation to solve the resulting finite-dimensional

NLP. The comparisons quantify the mathematical and computational effects of varying α and ψ.

6.2. Manufactured ψ-Caputo verification

Consider:

$$ {}^{C}D_{0+}^{\alpha,\psi}x(t) = u(t), \quad x(0) = 0, \tag{129} $$

with $\alpha = 0.85$ and the logarithmic clock in **Equation (53)**. Let $\theta = \Theta(t)$ be the normalized operational time defined in **Equation (6)**. In operational time, define the reference pullbacks:

$$ \widehat{u}^*(\theta) = \theta^6, \quad \widehat{x}^*(\theta) = \frac{\Gamma(7)}{\Gamma(\alpha+7)}\theta^{\alpha+6}. \tag{130} $$

The corresponding physical-time reference functions are $u^*(t) = \widehat{u}^*(\Theta(t))$ and $x^*(t) = \widehat{x}^*(\Theta(t))$. Because the normalized logarithmic clock satisfies $\Delta_\psi = 1$, **Theorem 1** gives:

$$ {}^{C}D_{0+}^{\alpha,\psi}x^*(t) = u^*(t), \quad x^*(0) = 0. \tag{131} $$

Thus, the pullback-defined reference pair satisfies **Equation (129)** as a direct consequence of the ψ-Caputo pullback identity in **Theorem 1**. Define the physical-time tracking functional:

$$ J = \int_0^1 \Big[\big(x(t) - x^*(t)\big)^2 + 0.2\big(u(t) - u^*(t)\big)^2\Big]\, dt, \tag{132} $$

where the cost J is defined in physical time, whereas the numerical errors reported in **Table 3** are computed in the normalized operational variable $\theta \in [0,1]$. Over the feasible set defined by **Equation (129)**, this nonnegative functional attains its unique minimum value $J = 0$, achieved at (x^*, u^*). **Table 3** and **Figure 2** show the numerical errors in operational time. For computational assessment, **Table 3** also reports the CPU time per complete benchmark computation, measured for each polynomial degree; J_N reports the computed objective value at degree N, and t_{CPU} represents the corresponding CPU time in seconds. At $N = 6$, the exact degree-six control belongs to the approximation space, and both the state and control errors decrease to approximately 10^{-15}. Thus, recovery to machine precision occurs once the degree-six control is contained in the approximation space.

Table 3. Manufactured-problem verification for $\alpha = 0.85$ and logarithmic clock

N	J_N	$\|\widehat{x}_N - \widehat{x}^*\|_\infty$	$\|\widehat{u}_N - \widehat{u}^*\|_\infty$	t_{CPU} (s)	r_{KKT}	$\kappa_2(H)$
2	1.08×10^{-3}	1.79×10^{-2}	1.95×10^{-1}	7.81×10^{-3}	1.55×10^{-17}	4.40
4	2.61×10^{-6}	6.23×10^{-4}	1.65×10^{-2}	1.33×10^{-2}	1.40×10^{-17}	7.35
6	4.11×10^{-32}	9.99×10^{-16}	1.55×10^{-15}	1.72×10^{-2}	1.97×10^{-17}	8.58
8	3.89×10^{-32}	9.71×10^{-16}	1.44×10^{-15}	1.88×10^{-2}	7.96×10^{-18}	9.11

6.3. Comparison with a recent robotic optimal-control method

To provide a direct numerical comparison with a recent state-of-the-art method, we also solve the planar free-flying robotic benchmark of Ghasempour *et al.*[21] using the same dynamics, initial conditions, performance index, integer-order case, and total root-mean-square (RMS) dynamic-residual definition. Ghasempour *et al.*[21] reported a total RMS dynamic residual of 3.29461×10^{-7} for $M = 4$ and $\eta = 1$, where M and η are the number of polynomials and fractional order, respectively, in the reference method. We apply the present method with $N = 4$ and $\alpha = 1$, as shown in **Table 4**. The present reduced-space reconstruction yields a near-machine-precision dynamic residual on this common benchmark. This behavior is consistent with the analytical state-reconstruction identities of the present formulation for $\alpha = 1$. The comparison is restricted to the common dynamic-residual measure; we do not compare objective values because the published robotic example does not report a corresponding objective value.

Table 4. Direct comparison on the robotic benchmark of Ghasempour *et al.*[21]

Method	Basis parameter	α or η	Total RMS dynamic residual
Ghasempour *et al.*[21]	$M = 4$	1	3.29461×10^{-7}
Present method	$N = 4$	1	1.1188×10^{-16}

6.4. Effect of operational clock on the linear regulator

Table 5 compares the four clocks for the linear regulator benchmark with $\alpha = 0.9$ and $N = 8$. The reported quantities are chosen to separate the main operational effects of ψ: the clock shape, through $\psi'(t)$ and $\chi'(\theta)$, describes the memory and cost-density distribution; the objective value J measures the complete physical-time cost; $\|z(1)\|_2$ measures terminal accuracy; E_u measures integrated control effort in physical time; and $U_{\max}$ measures peak actuation. The reported value of J is the complete two-axis objective in **Equation (45)**, including the running position, velocity, control terms, and terminal penalties. The terminal norm is:

$$\|z(1)\|_2 = \sqrt{x_1^2(1) + x_2^2(1) + v_1^2(1) + v_2^2(1)}, \tag{133}$$

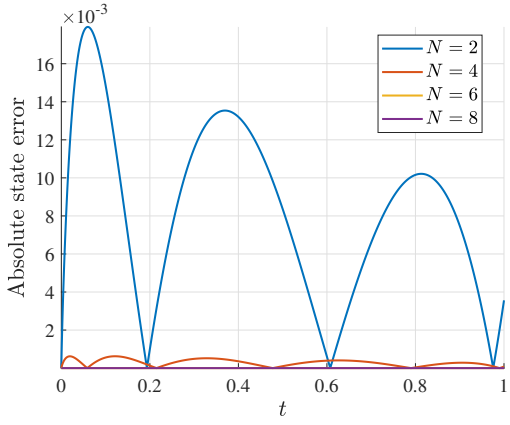
the physical-time control energy is:

$$E_u = \int_0^1 \left(u_1^2(t) + u_2^2(t)\right) dt, \tag{134}$$

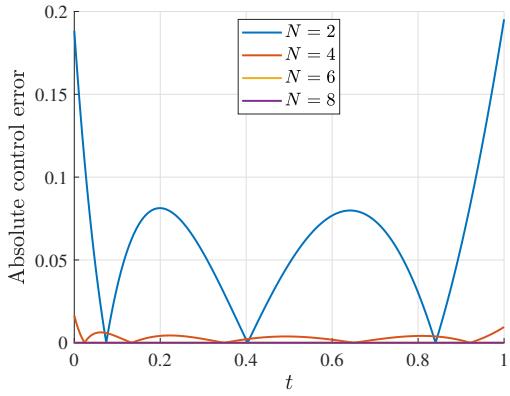
and the peak control magnitude is:

$$U_{\max} = \max_{\substack{t\in[0,1]\\ i\in\{1,2\}}} |u_i(t)|. \tag{135}$$

Note that the logarithmic clock is early-fast: it advances the operational memory clock rapidly near the beginning of the maneuver and then slows down. In the present linear regulator, this clock provides the lowest physical-time objective value and the lowest integrated control energy among the four cases; however, it also produces the largest terminal norm. On the other hand, the exponential clock is late-fast: it advances the operational memory clock slowly at first and rapidly near the terminal part of the maneuver. It produces the smallest terminal norm, but also the largest $U_{\max}$ and the highest objective value. These differences show that ψ controls an operational energy-accuracy tradeoff rather than a purely numerical parametrization.



(a) State error $|\widehat{x}_N - \widehat{x}^*|$



(b) Control error $|\widehat{u}_N - \widehat{u}^*|$

Figure 2. Operational-time absolute errors for the manufactured ψ-Caputo problem with $\alpha = 0.85$, logarithmic clock, and $N = 2, 4, 6, 8$

Table 5. Operational-clock comparison for the linear regulator with $\alpha = 0.9$ and $N = 8$

Clock	J	$\|z(1)\|_2$	E_u	$U_{\max}$	$\kappa_2(H)$
Identity	2.3187	0.2446	12.6977	5.5283	129.73
Logarithmic	1.7913	0.2820	10.8707	7.9897	303.10
Power	2.5273	0.2246	13.1790	6.7188	168.88
Exponential	2.7562	0.1802	12.6992	9.2297	284.15

Figures 3 and **4** show the corresponding physical-time trajectories and control channels. Although the operational-time dynamics retain the same Caputo form for all normalized clocks in the variable θ, the induced physical-time trajectories differ due to the clock-dependent mapping $t = \chi(\theta)$ and the cost-weight transformation. Under the operational-time pullback, $\chi'(\theta)$ acts directly on the running-cost density, including the control-effort density. It does not directly multiply the terminal penalty; however, changing the clock alters the optimal trajectory and, therefore, the terminal state reached at $t = 1$. For example, the induced Jacobian $\chi'(\theta)$ increases for the logarithmic clock and decreases for the exponential clock; hence, these two maps assign greater physical-time running-cost density to opposite regions of the operational interval. This produces different

early- and late-time control profiles. Hence, the same endpoint-normalized dynamics can lead to different memory distributions, control-effort distributions, terminal accuracies, and physical-time costs. The stationarity residual norms r_{KKT} for all four cases are below 4×10^{-15}. Therefore, the differences in **Table 5** are not caused by an inaccurate linear solve; they arise from the operational clock selected through ψ.

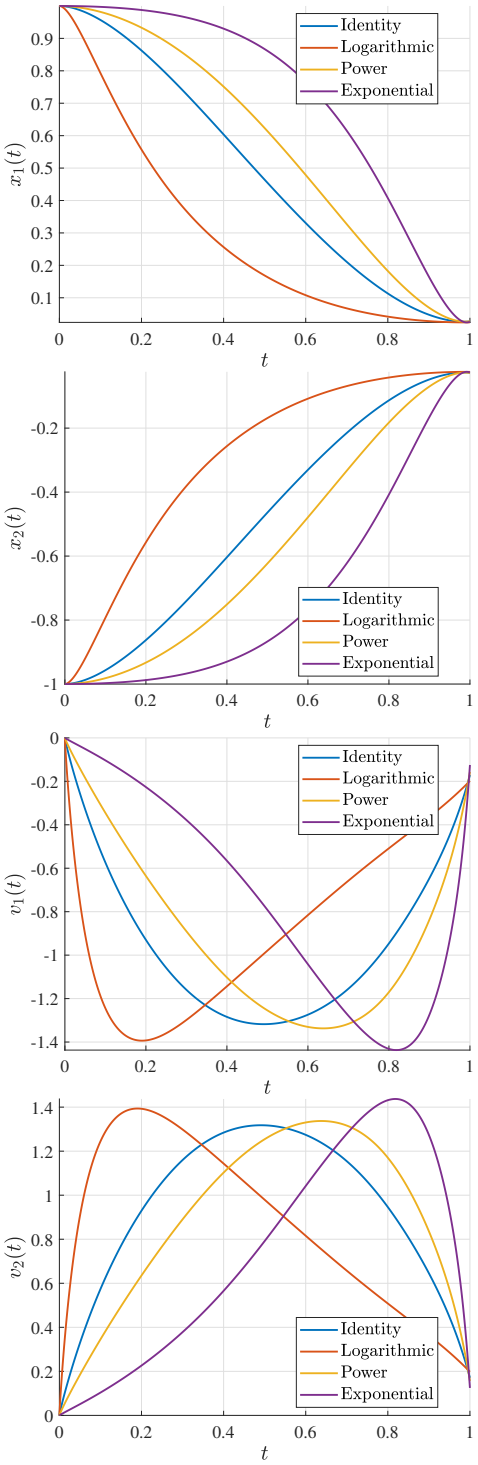


Figure 3. Physical-time state trajectories of the linear regulator for the identity, logarithmic, power, and exponential clocks with $\alpha = 0.9$ and $N = 8$

6.5. Continuous kernel-sensitivity study

To strengthen the kernel-selection analysis beyond the four isolated clocks in **Table 5**, we also consider the continuous normalized exponential family:

$$\psi_\rho(t) = \begin{cases} \dfrac{e^{\rho t} - 1}{e^{\rho} - 1}, & \rho \neq 0, \\ t, & \rho = 0. \end{cases} \tag{136}$$

This family satisfies $\psi_\rho(0) = 0$, $\psi_\rho(1) = 1$, and $\psi'_\rho(t) > 0$. Negative values of ρ generate concave, early-fast clocks for which $d\theta/dt$ is large near the beginning of the maneuver and then decreases. Positive values of ρ generate convex, late-fast clocks for which operational-time accumulation is delayed initially and accelerates near the end of the maneuver. The case $\rho = 0$ is the identity clock, while $\rho = 2$ coincides with the exponential clock used in **Table 5**.

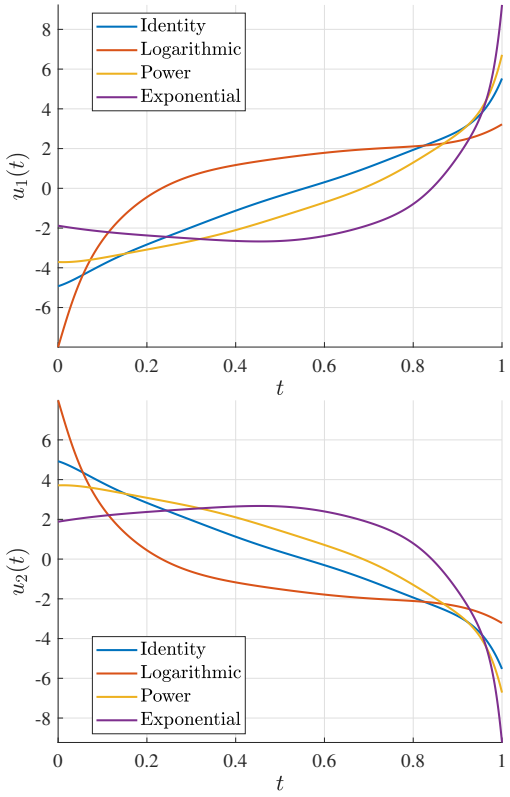


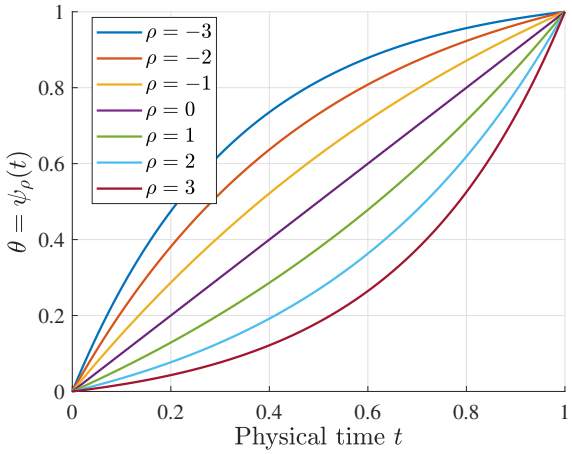
Figure 4. Physical-time optimal control channels of the linear regulator for the identity, logarithmic, power, and exponential clocks with $\alpha = 0.9$ and $N = 8$

Table 6 reports the resulting linear-regulator sensitivity sweep for $\rho = -3, -2, -1, 0, 1, 2, 3$. **Figure 5** shows the corresponding clocks and the main quantities normalized by the identity-clock case. The results show a systematic operational-clock tradeoff. Early-fast clocks with $\rho < 0$ place more operational-memory weight near the beginning of the physical maneuver; in the tested cases, this configuration reduces the objective value and the

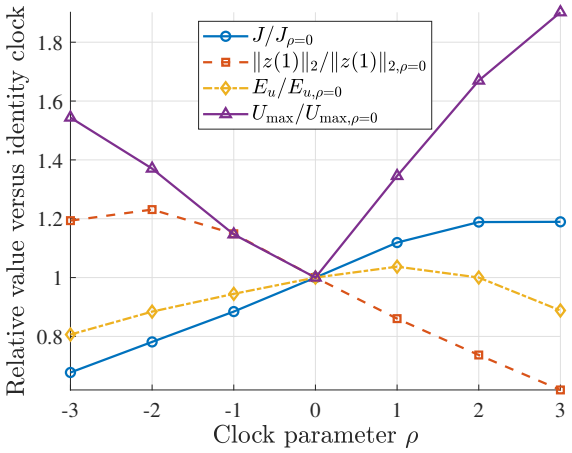
integrated control energy but increases the terminal norm relative to the identity clock. Late-fast clocks with $\rho > 0$ place more operational-memory weight near the terminal part of the maneuver; these clocks reduce the terminal norm, reaching approximately 62% of the identity-clock terminal norm at $\rho = 3$, but require larger peak control, reaching approximately 1.90 times the identity-clock peak control at $\rho = 3$. Thus, the kernel choice is not arbitrary: it shifts the controller between energy- or cost-dominant behavior and terminal-accuracy-dominant behavior by changing both the memory distribution and the Jacobian-weighted physical-time cost density. This continuous sensitivity study provides direct numerical evidence that ψ affects memory distribution, control effort, terminal accuracy, and physical-time cost and supports selecting the kernel based on the identified temporal-memory behavior and the task objective of the robotic system.

6.6. Fractional-order sensitivity in the linear regulator

Table 7 keeps the identity clock and varies α in the linear regulator benchmark. For the present normalized weights, decreasing α lowers the computed cost, control energy, and terminal norm, although $U_{\max}$ does not exhibit monotonic dependence on α. **Figure 6** also shows that changing α alters the physical-time profiles of both $\|z(t)\|_2$ and $\|u(t)\|_2$.



(a) Normalized clocks $\psi_\rho(t)$ for $\rho = -3, \ldots, 3$



(b) Objective value, terminal-state norm, control energy, and peak control normalized by their identity-clock values

Figure 5. Continuous sensitivity of the linear-regulator solution to the normalized exponential-clock parameter ρ

Table 6. Continuous ψ_ρ-kernel sensitivity for the linear regulator with $\alpha = 0.9$ and $N = 8$

ρ	Clock type	J	$\|z(1)\|_2$	E_u	$U_{\max}$	$\kappa_2(H)$
-3	Strong early-fast	1.5707	0.2920	10.2383	8.5347	394.75
-2	Mild early-fast	1.8116	0.3011	11.2280	7.5759	290.00
-1	Mild early-fast	2.0507	0.2810	11.9956	6.3403	200.14
0	Uniform identity	2.3187	0.2446	12.6977	5.5283	129.73
1	Mild late-fast	2.5946	0.2105	13.1685	7.4374	197.55
2	Mild late-fast	2.7562	0.1802	12.6992	9.2297	284.15
3	Strong late-fast	2.7581	0.1512	11.2775	10.5134	385.02

Table 7. Order comparison for the linear regulator with the identity clock and $N = 8$

α	J	$\|z(1)\|_2$	E_u	$U_{\max}$	$\kappa_2(H)$
1.0	3.0160	0.3284	17.3933	5.9464	101.21
0.9	2.3187	0.2446	12.6977	5.5283	129.73
0.8	1.8089	0.1756	9.3047	6.2804	162.24
0.7	1.4297	0.1202	6.8926	6.5905	197.37

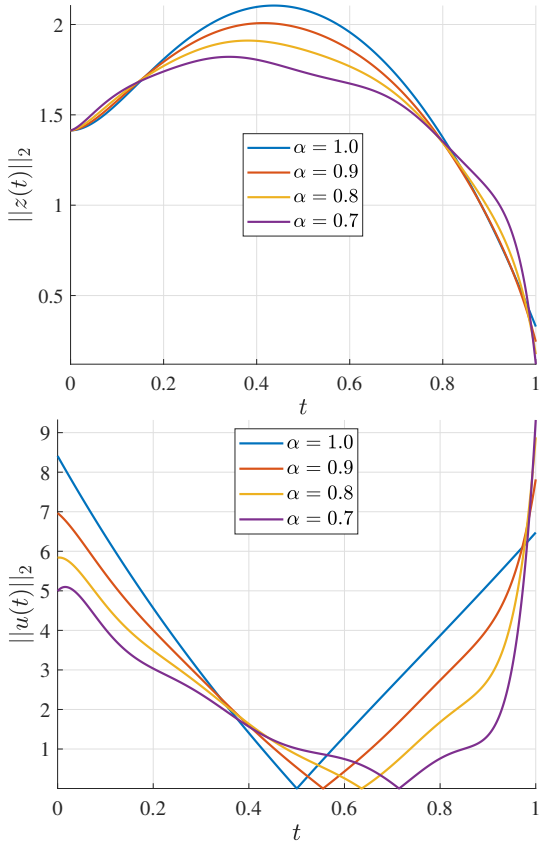


Figure 6. Fractional-order sensitivity of the linear regulator under the identity clock with $N = 8$ and $\alpha = 1.0, 0.9, 0.8, 0.7$

6.7. Basis-refinement study for the linear regulator

Table 8 and **Figure 7** compare degrees $N = 2$ through $N = 8$ for the linear regulator benchmark with $\alpha = 0.9$ and the identity clock. Using the $N = 8$ computation as the numerical reference, we define:

$$\delta_J(N) = \frac{|J_N - J_8|}{J_8},$$
$$\delta_u(N) = \left(\int_0^1 |u_{1,N}(t) - u_{1,8}(t)|^2 \, dt \right)^{1/2}, \quad (137)$$

where $u_{1,N}(t)$ is the first physical-time control channel computed with polynomial degree N. Because the identity clock is used, the physical-time and operational-time L^2 measures coincide. However, the objective value stabilizes faster than the control function. This behavior is consistent with a strictly convex quadratic structure. Once the first-order optimality condition is satisfied at the reference minimizer, the objective gap exhibits second-order scaling with respect to perturbations measured in the Hessian-induced energy norm. Consequently, the objective can appear numerically converged even while a visible difference in the control function remains.

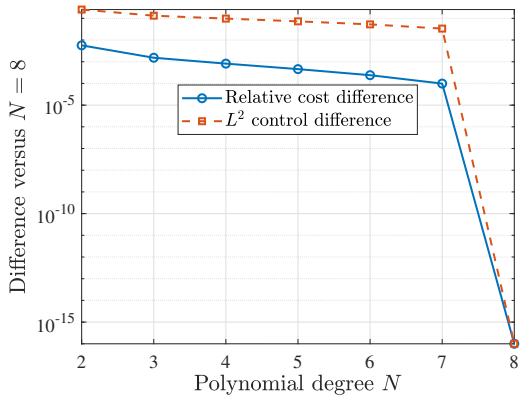


Figure 7. Mittag-Leffler basis-refinement behavior for the linear regulator with $\alpha = 0.9$ and the identity clock

Table 8. Basis refinement for the linear regulator with $\alpha = 0.9$ and the identity clock

N	J_N	$\delta_J(N)$	$\delta_u(N)$	$\|z(1)\|_2$	$\kappa_2(H)$
2	2.3319	5.68×10^{-3}	0.2541	0.2478	120.69
3	2.3223	1.53×10^{-3}	0.1326	0.2456	126.86
4	2.3206	8.19×10^{-4}	0.0973	0.2452	128.53
5	2.3198	4.57×10^{-4}	0.0727	0.2449	129.14
6	2.3193	2.40×10^{-4}	0.0527	0.2448	129.46
7	2.3189	9.84×10^{-5}	0.0337	0.2447	129.62
8	2.3187	0	0	0.24461	129.73

6.8. Nonlinear two-link manipulator validation

The preceding robotic results demonstrate the linear-regulator case in which exact state elimination yields a symmetric positive-definite quadratic program. To demonstrate numerical applicability beyond this simplified benchmark, we now solve the nonlinear manipulator problem in **Equations (57)–(64)**. The fractional order is fixed at $\alpha = 0.9$, and the four normalized clocks in **Equations (52)–(55)** are compared. The terminal joint error and terminal velocity norm are

defined as follows:

$$e_q = \|q(1) - q_f\|_2, \quad e_\omega = \|\omega(1)\|_2, \tag{138}$$

the torque energy is:

$$E_\tau = \int_0^1 \left(\tau_1^2(t) + \tau_2^2(t)\right) dt, \tag{139}$$

and the peak torque magnitude is:

$$\tau_{\max} = \max_{\substack{t\in[0,1]\\ i\in\{1,2\}}} |\tau_i(t)|. \tag{140}$$

To verify the nonlinear discretization between the collocation nodes, the acceleration-equation defect is also evaluated independently on the 4001-point uniform operational-time grid $\mathcal{G}_d \subset [0,1]$. Its scale-normalized maximum is:

$$R_{d,\mathrm{rel}} = \frac{\max_{\theta\in\mathcal{G}_d} \|d_N(\theta)\|_\infty}{S_d}, \tag{141}$$

where:

$$d_N(\theta) = \widehat{r}_{\omega,N}(\theta) - f_m\big(\widehat{q}_N(\theta), \widehat{\omega}_N(\theta), \widehat{\tau}_N(\theta)\big), \tag{142}$$

and:

$$S_d = \max\Big\{1, \max_{\theta\in\mathcal{G}_d} \|\widehat{r}_{\omega,N}(\theta)\|_\infty, \max_{\theta\in\mathcal{G}_d} \big\| f_m\big(\widehat{q}_N(\theta), \widehat{\omega}_N(\theta), \widehat{\tau}_N(\theta)\big)\big\|_\infty\Big\}. \tag{143}$$

Let R_c denote the maximum absolute residual at the imposed collocation nodes. Polynomial refinement yields the first common resolution for which all four clocks satisfy the sequential quadratic programming convergence condition, $R_c \le 10^{-7}$, $R_{d,\mathrm{rel}} \le 2\times10^{-2}$, and a relative objective change below 5×10^{-3} from the preceding polynomial degree; this occurs at $N = 13$ and $n_c = 14$. At this resolution, the maximum collocation residual among the four clocks is 5.68×10^{-14}, the maximum dense relative residual is 1.88×10^{-2}, and the maximum relative objective change from the preceding degree $N = 11$ is 2.66×10^{-3}. **Table 9** reports the resulting nonlinear-programming results. The columns e_q and e_ω measure terminal accuracy, whereas E_τ and $\tau_{\max}$ measure integrated and peak control effort. The different values of J_m, e_q, e_ω, E_τ, and $\tau_{\max}$ again reflect the operational-clock effect of ψ: the clock redistributes the fractional memory in the nonlinear dynamics and weights the physical-time running cost through $\chi'(\theta)$.

Figure 8 shows representative joint and torque profiles for the identity clock and the end-effector paths obtained with all four clocks using the forward kinematics in **Equation (63)**. The initial end-effector point is $p(q(0)) = (2,0)$, and the target point corresponds to $p(q_f)$ with $q_f = [\pi/3, -\pi/4]^\mathsf{T}$. The end-effector plot uses the same clock ordering as the legend: identity, logarithmic, power, and exponential. The plots confirm that the proposed discretization can be applied directly to a nonlinear robotic model with actuator torques; however, the resulting finite-dimensional problem is nonlinear rather than a symmetric positive-definite quadratic program.

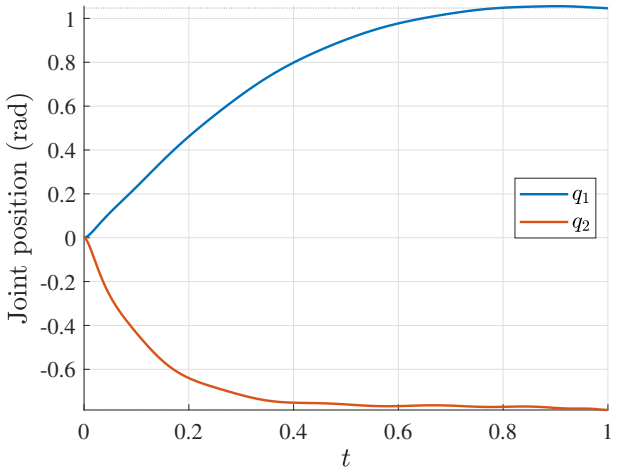
Table 9. Nonlinear two-link manipulator validation with $\alpha = 0.9$, $N = 13$, and $n_c = 14$

Clock	J_m	e_q	e_ω	E_τ	$\tau_{\max}$	R_c
Identity	11.4777	1.74×10^{-3}	1.66×10^{-2}	381.99	59.43	4.35×10^{-14}
Logarithmic	6.0907	3.69×10^{-3}	3.80×10^{-2}	229.33	71.07	3.55×10^{-14}
Power	14.6366	2.82×10^{-3}	9.78×10^{-3}	457.59	51.20	5.68×10^{-14}
Exponential	21.0940	4.16×10^{-3}	1.14×10^{-3}	551.74	34.20	3.33×10^{-14}

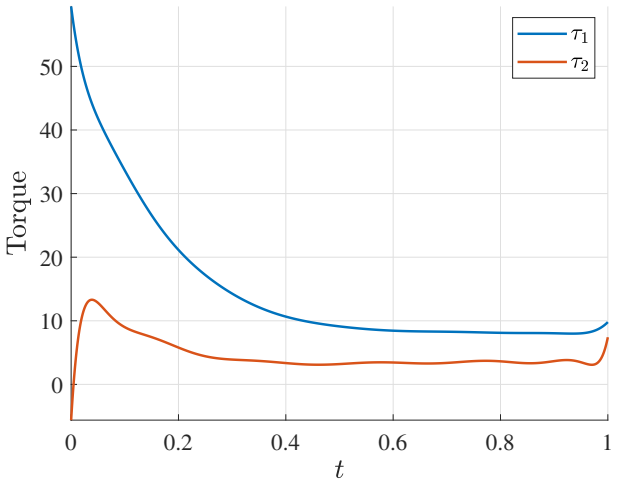
6.9. Interpretation of the kernel and selection guideline

The operational effects of ψ on memory distribution, physical-time cost weighting, control-effort allocation, and terminal accuracy have already been established in Section 3 through **Equations (39)** and **(40)**. The present subsection therefore focuses on the practical interpretation and selection of the kernel. The physical suitability of a kernel should be interpreted through the shape of $\psi'(t)$, not through the objective value alone. **Table 10** summarizes the engineering interpretation of the representative clocks used in this study. A uniform clock is appropriate when no evidence of nonuniform memory accumulation is available. An early-fast clock is appropriate when the dominant memory or relaxation effects occur near the beginning of the motion, such as start-up transients, breakaway friction, or rapid initial compliance relaxation. A late-fast clock is appropriate when the dominant memory effect becomes stronger near the end of the maneuver, such as terminal contact, near-target precision, or delayed actuation

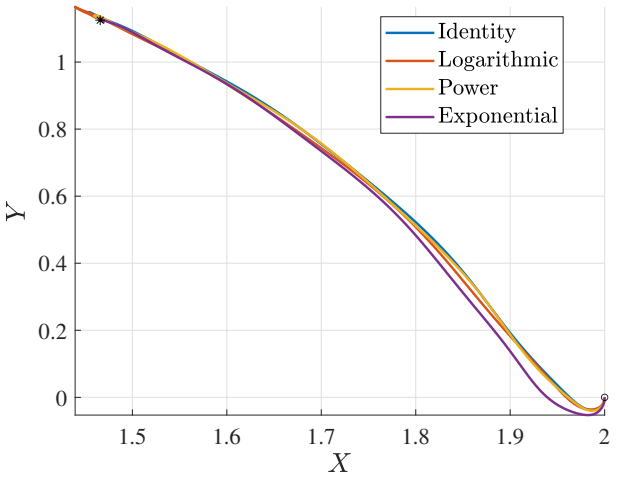
effects. The power and exponential clocks represent moderate and strong versions of late-fast memory accumulation, respectively.



(a) Joint trajectories $q_1(t)$ and $q_2(t)$ for the identity clock



(b) Actuator torques $\tau_1(t)$ and $\tau_2(t)$ for the identity clock



(c) Physical-plane end-effector paths for the identity, logarithmic, power, and exponential clocks

Figure 8. Nonlinear two-link manipulator validation with $\alpha = 0.9$, $N = 13$, and $n_c = 14$

In an experimental robotic application, the clock should be selected by system identification or validation. If input-output data $\{u(t_k), y_{\exp}(t_k)\}_{k=1}^{N_d}$ are available, where t_k are the sampling times, $y_{\exp}(t_k)$ are the measured outputs, and N_d is the number of data samples, the fractional order and kernel parameters can be estimated from the following:

$$(\alpha^*, \xi^*) = \arg\min_{\alpha,\xi} \left[\mathcal{E}_{\text{fit}}(\alpha, \xi) + \lambda_{\text{reg}} \mathcal{R}(\xi)\right],$$
$$\mathcal{E}_{\text{fit}}(\alpha, \xi) = \sum_{k=1}^{N_d} \left\| y_{\exp}(t_k) - h(z_{\alpha,\xi}(t_k)) \right\|^2. \tag{144}$$

The minimization in **Equation 144** is subject to the ψ_ξ-Caputo robotic model, the normalization constraints $\psi_\xi(0) = 0$, $\psi_\xi(T) = 1$, and the monotonicity constraint $\psi'_\xi(t) > 0$. Here, ξ denotes the kernel parameters, $h(\cdot)$ is the measurement map, and $\mathcal{R}$ is a regularization term used to avoid overfitting. Moreover, $\mathcal{E}_{\text{fit}}$ denotes the data-fitting error, $\lambda_{\text{reg}} \geq 0$ is the regularization weight, and $z_{\alpha,\xi}$ is the model state obtained for the fractional order α and kernel parameter ξ. The physically appropriate kernel is the one that yields the best validation accuracy and a consistent residual structure, not necessarily the lowest simulated optimal-control cost.

Regarding robustness, the numerical studies in this work use nominal model parameters and deterministic data and therefore should not be interpreted as a stochastic or worst-case robustness analysis. Nevertheless, the sensitivity of the linear reduced problem to small parameter perturbations can be characterized directly. Let perturbations in the assembled model and cost data produce $H + \Delta H$ and $g + \Delta g$, with corresponding solution $c^* + \Delta c$. From $Hc^* = -g$, one obtains:

$$(H + \Delta H)\Delta c = -\left(\Delta g + \Delta H\, c^*\right). \tag{145}$$

Hence, provided that $H + \Delta H$ remains positive definite:

$$\|\Delta c\|_2 \leq \left\|(H + \Delta H)^{-1}\right\|_2 \times \left(\|\Delta g\|_2 + \|\Delta H\|_2 \|c^*\|_2\right). \tag{146}$$

Thus, sensitivity to small parameter perturbations is governed by the conditioning of the reduced algebraic system, which motivates the reported values of $\kappa_2(H)$. For noisy experimental data, the regularization term in **Equation (144)**, together with validation-based kernel selection, limits overfitting. However, the present deterministic simulations do not establish a statistical noise-robustness guarantee; a full stochastic or robust optimal-control treatment is beyond the scope of the present study.

Table 10. Engineering interpretation of the representative ψ-kernels.

Clock	Physical interpretation and selection evidence
Identity	Constant $\psi'(t)$. Suitable as a baseline rigid or weak-memory model when validation data do not indicate non-uniform temporal memory.
Logarithmic	Early-fast clock with a large initial $\psi'(t)$ followed by a decreasing rate. Suitable for start-up transients, breakaway friction, and rapid initial compliance or actuator relaxation; selected when identity-clock residuals are mainly early-time residuals.
Power	Moderately late-fast clock with increasing $\psi'(t)$. Suitable for gradually increasing load, contact influence, or task difficulty; selected when validation error improves under mild late-time clock acceleration.
Exponential	Strong late-fast clock with rapidly increasing $\psi'(t)$. Suitable for terminal contact, near-target precision, delayed actuation, or end-of-maneuver effects; selected when identity-clock residuals are mainly late-time residuals.

7. Conclusion

This study presented a unified kernel-adaptive framework for the optimal control of robotic systems governed by ψ-Caputo fractional dynamics. Relative to fixed-kernel FOCPs, spectral/polynomial approximation schemes, and fractional LQ methods with prescribed kernels, the main novelty lies in integrating a nonlinear operational clock, a Jacobian-consistent physical-time objective, and a QR-stabilized Mittag-Leffler polynomial discretization. By transforming the problem into normalized operational time while preserving the physical-time cost through the Jacobian weight, the proposed formulation clarified the role of ψ as a nonlinear operational clock. A QR-stabilized Mittag-Leffler polynomial basis and analytical fractional integration were used to eliminate the state variables in the linear planar regulator, thereby reducing that benchmark problem to a symmetric positive-definite quadratic system with a unique solution. For the nonlinear two-link manipulator, the same operational-time and basis framework led instead to a finite-dimensional NLP problem, which was solved by direct collocation. The manufactured benchmark confirmed near-machine-precision reconstruction when the exact control belonged to the approximation space, while the regulator refinement results demonstrated numerical convergence and stability. The nonlinear manipulator example further demonstrated the applicability of the proposed framework to configuration-dependent robotic dynamics, including Coriolis/centrifugal effects, gravity, damping, and actuator torques. Comparisons among the identity, logarithmic, power, and exponential clocks in the examples considered showed that ψ acts as an operational clock: it redistributes memory and, through the Jacobian-weighted physical-time objective, changes the control-effort distribution, terminal accuracy, total physical-time cost, and torque profiles. The continuous ψ_ρ sensitivity sweep further showed that early-fast clocks can reduce the objective value and energy but increase terminal error; in contrast, late-fast clocks improve terminal accuracy but require larger peak actuation. From a practical viewpoint, these results indicate that ψ can be selected as a task-dependent operational clock to balance control energy, terminal accuracy, and peak actuation according to the temporal-memory characteristics of the robotic system. The present framework, however, has some limitations: the admissible clocks are restricted to C^1 strictly increasing functions with $\psi'(t) > 0$; the symmetric positive-definite reduction and the convergence result are established for the unconstrained linear regulator, with **Theorem 2** assuming $1/2 < \alpha \leq 1$; and the current simulations use nominal deterministic models without experimental validation or stochastic robustness guarantees. Future work should extend the framework to more general nonlinear robotic systems with state and input constraints, uncertain parameters, and more complex coupled or contact dynamics, together with data-driven kernel identification, receding-horizon control, and experimental validation.

Acknowledgments

None.

Funding

None.

Conflict of interest

The authors declare they have no competing interests.

Author contributions

Conceptualization: All authors
Methodology: Amin Jajarmi
Software: Amin Jajarmi
Supervision: Dumitru Baleanu
Validation: Dumitru Baleanu
Writing – original draft: Amin Jajarmi
Writing – review & editing: Dumitru Baleanu

Availability of data

No data was used for the research described in the article.

AI tools statement

All authors confirm that no AI tools were used in the preparation of this manuscript.

References

1. Tassaddiq A, Qureshi S, Soomro A, Abu Arqub O, Senol M. Comparative analysis of classical and Caputo models for COVID-19 spread: vaccination and stability assessment. *Fixed Point Theory Algorithms Sci Eng.* 2024;2024:2. https://doi.org/10.1186/s13663-024-00760-7

2. Qureshi S. Fox H-functions as exact solutions for Caputo type mass spring damper system under Sumudu transform. *J Appl Math Comput Mech.* 2021;20(1):83-89. https://doi.org/10.17512/jamcm.2021.1.08

3. Samko SG, Kilbas AA, Marichev OI. *Fractional Integrals and Derivatives: Theory and Applications*. Yverdon, Switzerland: Gordon and Breach Science Publishers; 1993.

4. Baleanu D, Diethelm K, Scalas E, Trujillo JJ. *Fractional Calculus: Models and Numerical Methods*. Vol 3. Singapore: World Scientific; 2012. https://doi.org/10.1142/8180

5. Agrawal OP. A general formulation and solution scheme for fractional optimal control problems. *Nonlinear Dyn.* 2004;38(1-4):323-337. https://doi.org/10.1007/s11071-004-3764-6

6. Baleanu D, Tajani A, Zguaid K, Jajarmi A. Fractional optimal control problems in the sense of ψ-Caputo fractional derivative. *Optim Control Appl Methods.* 2025;46(6):2867-2881. https://doi.org/10.1002/oca.70034

7. Alqhtani M, Sadek L, Saad KM. The Mittag-Leffler-Caputo-Fabrizio fractional derivative and its numerical approach. *Symmetry.* 2025;17(5):800. https://doi.org/10.3390/sym17050800

8. Sadek L, Aldawish I. An efficient numerical approach for solving the Mittag-Leffler fractional differential equations. *Math Sci.* 2026;20(3):263-280. https://doi.org/10.57647/mathsci.2026.2003.14

9. Zaky MA, Doha EH. A new adaptive spectral collocation method for tempered fractional differential equations with initial singularities. *Comput Appl Math.* 2026;45(7):302. https://doi.org/10.1007/s40314-026-03699-0

10. Ahmed AI. Collocation method for solving delay fractional optimal control problems by fractional-order Chelyshkov functions. *Adv Cont Discr Mod.* 2026;2026:24. https://doi.org/10.1186/s13662-026-04065-4

11. Qureshi S, Argyros IK, Ramos H, *et al.* A stable optimal solver for nonlinear equations with semilocal convergence using majorizing sequences in Banach spaces. *SeMA J.* 2026;83:515-549. https://doi.org/10.1007/s40324-025-00402-x

12. Jmal A, Ahmed H. Generalized Mittag-Leffler stability for k-Caputo fractional-order systems—An observer application. *Asian J Control.* 2026;28(1):424-430. https://doi.org/10.1002/asjc.3754

13. Ma L, Zhang W. Finite-time stability for Caputo-Hadamard type fractional differential systems without and with proportional delays. *Chaos.* 2026;36(1):013131. https://doi.org/10.1063/5.0311074

14. Ghosh I, Cheong HT, Teo KL. A novel gradient-based discrete time-delayed optimization algorithm for optimal control problems with Caputo-Fabrizio fractional derivative. *J Comput Appl Math.* 2025;464:116526. https://doi.org/10.1016/j.cam.2025.116526

15. Hidayatullah AA, Subchan S, Safarina S, *et al.* A hybrid fractional Chebyshev-Legendre spectral collocation method for Hamilton-Jacobi-Bellman equations. *IEEE Access.* 2026;14:34564-34584. https://doi.org/10.1109/ACCESS.2026.3668899

16. Sadek L, Samei ME, Hashemi MS. The Galerkin Mittag-Leffler method for solving fractional optimal control problems with inequality constraints. *Math Comput Simul.* 2026;240:191-207. https://doi.org/10.1016/j.matcom.2025.07.018

17. Sadek L, Aldawish I, Hammouch Z, Shafee A, Popa IL. A robust Galerkin fractional Taylor technique to solve multi-dimensional fractional optimal control problems with inequality constraints. *Math Sci.* 2026;20(4):359-375. https://doi.org/10.57647/mathsci.89bj.w891

18. Mao X, Wang X, Lu Y, Qin H. Synchronizations control of fractional-order multidimension-valued

memristive neural networks with delays. *Neurocomputing.* 2024;563:126942. https://doi.org/10.1016/j.neucom.2023.126942

19. Chávez-Vázquez S, Gómez-Aguilar JF, Lavín-Delgado JE, Escobar-Jiménez RF, Olivares-Peregrino VH. Applications of fractional operators in robotics: A review. *J Intell Robot Syst.* 2022;104(4):63. https://doi.org/10.1007/s10846-022-01597-1

20. Singh AP, Bingi K. Applications of fractional-order calculus in robotics. *Fractal Fract.* 2024;8(7):403. https://doi.org/10.3390/fractalfract8070403

21. Ghasempour A, Ordokhani Y, Razzaghi M. An efficient optimal control framework for robotic systems using Mittag-Leffler polynomial techniques. *Optim Control Appl Methods.* 2026;47(4):1004-1014. https://doi.org/10.1002/oca.70110

22. Odibat Z, Qureshi S, Cattani C, Gómez-Aguilar JF, Yang XJ, Baleanu D. Analytical solutions of fractional Burgers' equation with exponential extension kernel derivatives. *J Comput Appl Math.* 2026;486:117620. https://doi.org/10.1016/j.cam.2026.117620

23. Saad KM, Abdo MS, Hamanah WM. Existence and controllability analysis of multi-term fractional coupled systems with generalized $[\psi, w]$-Caputo-Fabrizio operators. *Sci Rep.* 2025;15:34434. https://doi.org/10.1038/s41598-025-17523-y

24. Almeida R. A Caputo fractional derivative of a function with respect to another function. *Commun Nonlinear Sci Numer Simul.* 2017;44:460-481. https://doi.org/10.1016/j.cnsns.2016.09.006

25. Sousa JVC, Oliveira EC de. On the ψ-Hilfer fractional derivative. *Commun Nonlinear Sci Numer Simul.* 2018;60:72-91. https://doi.org/10.1016/j.cnsns.2018.01.005

26. Almeida R. What is the best fractional derivative to fit data? *Appl Anal Discrete Math.* 2017;11(2):358-368. https://doi.org/10.2298/AADM170428002A

27. Baghani O. Solving state feedback control of fractional linear quadratic regulator systems using triangular functions. *Commun Nonlinear Sci Numer Simul.* 2019;73:319-337. https://doi.org/10.1016/j.cnsns.2019.01.023

28. Gomoyunov MI. Value functional and optimal feedback control in linear-quadratic optimal control problem for fractional-order system. *Math Control Relat Fields.* 2024;14(1):215-254. https://doi.org/10.3934/mcrf.2023002

29. Zhou B, Speyer JL. Fractional linear quadratic regulators using Wiener-Hopf spectral factorization. *SIAM J Control Optim.* 2019;57(6):4011-4032. https://doi.org/10.1137/19M1239520

30. Kilbas AA, Srivastava HM, Trujillo JJ. *Theory and Applications of Fractional Differential Equations.* North-Holland Mathematics Studies. Vol 204. Amsterdam: Elsevier; 2006. https://doi.org/10.1016/S0304-0208(06)80001-0

31. Qureshi S, Yusuf A, Aziz S. On the use of Mohand integral transform for solving fractional-order classical Caputo differential equations. *J Appl Math Comput Mech.* 2020;19(3):99-109. https://doi.org/10.17512/jamcm.2020.3.08

32. Mohiuddin M, Karim ME, Amin MR, *et al.* Detecting dynamical behaviors of solitary waves in the M-fractional Konopelchenko-Dubrovsky system with stability and sensitivity analysis. *Phys Open.* 2026;28:100454. https://doi.org/10.1016/j.physo.2026.100454

33. Alam N, Ullah MS, Manafian J, *et al.* Bifurcation analysis, chaotic behaviors, and explicit solutions for a fractional two-mode Nizhnik-Novikov-Veselov equation in mathematical physics. *AIMS Math.* 2025;10(3):4558-4578. https://doi.org/10.3934/math.2025211

34. Amin MR, Hakim MA, Ullah MS. Analysis of soliton behavior and overlap phenomena in the integrable beta-fractional Akbota equation with stability evaluation of equilibrium points. *AIP Adv.* 2025;15(12):125205. https://doi.org/10.1063/5.0308937

35. Gambo YY, Jarad F, Baleanu D, Abdeljawad T. On Caputo modification of the Hadamard fractional derivatives. *Adv Differ Equ.* 2014;2014:10. https://doi.org/10.1186/1687-1847-2014-10

36. Roman S. *The Umbral Calculus.* Orlando: Academic Press; 1984. https://books.google.com/books/about/The_Umbral_Calculus.html?id=JpHjkhFLfpgC

37. Spong MW, Hutchinson S, Vidyasagar M. *Robot Modeling and Control.* Hoboken: John Wiley & Sons; 2006. https://www.wiley.com/en-us/shop/general-introductory-electrical-electronics-engineering/robot-modeling-and-control-2nd-edition-p-9781119524045

Amin Jajarmi *received his B.Sc., M.Sc., and Ph.D. in electrical engineering from Ferdowsi University of Mashhad in 2005, 2007, and 2012, respectively. He is currently an associate professor in the Department of Electrical Engineering at the University of Bojnord, Iran, and an adjunct faculty member in the Department of Mathematics at Saveetha School of Engineering, SIMATS, Saveetha University, India. His research interests include computational methods for optimal*

control of nonlinear and fractional-order systems.
https://orcid.org/0000-0003-2768-840X

Dumitru Baleanu *is a professor in the Department of Computer Science and Mathematics, at Lebanese American University, Beirut, Lebanon, and the Institute of Space Sciences, Magurele, Bucharest, Romania. His fields of interest include fractional dynamics and their applications in science and engineering, fractional differential equations, discrete mathematics, mathematical physics, soliton theory, Lie symmetry, dynamical systems on time scales, and wavelet methods and their applications.*
https://orcid.org/0000-0002-0286-7244

An International Journal of Optimization and Control: Theories & Applications (https://accscience.com/journal/ijocta)

This work is licensed under a Creative Commons Attribution 4.0 International License. The authors retain ownership of the copyright for their article, but they allow anyone to download, reuse, reprint, modify, distribute, and/or copy articles in IJOCTA, so long as the original authors and source are credited. To see the complete license contents, please visit http://creativecommons.org/licenses/by/4.0/.